JOURNAL OF SPACECRAFT AND ROCKETS
Vol. 54, No. 3, May–June 2017

Laser-Guide-Star Satellite for Ground-Based Adaptive Optics Imaging of Geosynchronous Satellites

Weston A. Marlow,* Ashley K. Carlton,† Hyosang Yoon,† James R. Clark,†
Christian A. Haughwout,‡ and Kerri L. Cahoy§
Massachusetts Institute of Technology, Cambridge, Massachusetts 02139
and
Jared R. Males,¶ Laird M. Close,** and Katie M. Morzinski††
University of Arizona, Tucson, Arizona 85721

DOI: 10.2514/1.A33680

In this study, the feasibility and utility of using a maneuverable nanosatellite laser guide star from a geostationary equatorial orbit have been assessed to enable ground-based, adaptive optics imaging of geosynchronous satellites with next-generation extremely large telescopes. The concept for a satellite guide star was first discussed in the literature by Greenaway and Clark in the early 1990s ("PHAROS: An Agile Satellite-Borne Laser Guidestar," *Proceedings of SPIE*, Vol. 2120, 1994, pp. 206–210), and expanded upon by Albert in 2012 ("Satellite-Mounted Light Sources as Photometric Calibration Standards for Ground-Based Telescopes," *Astronomical Journal*, Vol. 143, No. 1, 2012, p. 8). With a satellite-based laser as an adaptive optics guide star, the source laser does not need to scatter, and is well above atmospheric turbulence. When viewed from the ground through a turbulent atmosphere, the angular size of the satellite guide star is much smaller than a backscattered source. Advances in small-satellite technology and capability allowed the revisiting of the concept on a 6U CubeSat, measuring $10 \times 20 \times 30$ cm. It is shown that a system that uses a satellite-based laser transmitter can be relatively low power (~1 W transmit power) and operated intermittently. Although the preliminary analysis indicates that a single satellite guide star cannot be used for observing multiple astronomical targets, it will only require a little propellant to relocate within the geosynchronous belt. Results of a design study on the feasibility of a small-satellite guide star have been presented, and the potential benefits to astronomical imaging and to the larger space situational awareness community have been highlighted.

Nomenclature

a_f	=	fitting-error constant
D	=	diameter, m
d	=	Euclidian distance, m
$F(\lambda)$	=	flux in a filter, photons $\cdot$ m^{-2} $\cdot$ s^{-1}
H	=	turbulence characteristic height, measured from sea level, m
h	=	orbit altitude, km
m	=	apparent stellar magnitude
r_s	=	actuator spacing as projected onto primary mirror, m
r_0	=	Fried's parameter, turbulence characteristic scale, m
r_{0V}	=	r_0, measured in V, a common reference value, m
$\bar{v}$	=	weighted mean wind speed, weighted by turbulence strength, m/s
Δt	=	servo lag, s
ΔV	=	change in velocity magnitude, m/s
θ	=	isoplanatic patch angle, arcsec
θ_z	=	telescope zenith angle measured from vertical, deg
λ	=	wavelength, m, μm, nm
λ_V	=	central wavelength of V band (here taken to be 550 nm)
λ_{WFS}	=	wavelength of the wave-front sensor, nm
τ_{exp}	=	wave-front-sensor exposure time, s
ϕ	=	beamwidth, rad

Received 23 June 2016; revision received 7 November 2016; accepted for publication 5 December 2016; published online 16 March 2017.

*Ph.D. Candidate, MIT Department of Aeronautics and Astronautics, 77 Massachusetts Avenue. Member AIAA.
†Ph.D. Candidate, MIT Department of Aeronautics and Astronautics. Student Member AIAA.
‡Graduate Student, MIT Department of Aeronautics and Astronautics. Student Member AIAA.
§Assistant Professor, MIT Department of Aeronautics and Astronautics. Member AIAA.
¶NASA Sagan Postdoctoral Fellow, Steward Observatory, 933 North Cherry Avenue.
**Associate Professor, Department of Astronomy and the Steward Observatory, 933 North Cherry Avenue.
††MagAO Instrument Scientist, Steward Observatory, 933 North Cherry Avenue.

I. Introduction

IMAGING of space-based assets and astronomical objects from large, ground-based observatories is inherently limited by atmospheric turbulence. The turbulent motion of the air between a telescope and space causes index of refraction variations, which corrupt the incoming wave front. This causes the image of a point source to blur, an effect referred to as "seeing." Seeing is usually quantified in terms of the full-width at half-maximum (FWHM) of the resultant image of a star. Typical values at astronomical observatories range from 0.5 to 1.0″ in visible wavelengths [1,2]. Importantly, this is true independent of telescope size. For an optimally performing telescope [i.e., diffraction limited, as discussed in Sec. III.A and described in Eq. (1)], we can compare seeing to the FWHM of the point-spread function (PSF) if a telescope were diffraction limited, and find that seeing is many times worse than diffraction-limited performance. In this case, FWHM is approximately λ/D, in which D is the diameter of the telescope and λ is the wavelength, neglecting details associated with pupil geometry. For the current generation of 6–10 m telescopes, the seeing-limited FWHM is 30–90 times larger than the limit set by diffraction. This difference in FWHM means that, without compensation, there will be a dramatic loss in angular resolution. This gap will be even larger on the next generation of 24–40 m extremely large telescopes (ELTs), in which the diffraction-limited FWHM is further reduced (improved).

In addition to degrading angular resolution, imaging through turbulence results in a loss of sensitivity. The larger PSF size increases the amount of background noise present in a measurement. When combined with the increased collecting area, the point-source

sensitivity of a diffraction-limited telescope is proportional to D^4, as opposed to D^2 in the seeing limit [3].

The atmosphere can be avoided entirely by putting telescopes in space, as in the case of the 2.4-m-diam Hubble Space Telescope (HST) and the planned 6.5 m James Webb Space Telescope (JWST) [4]. However, the launch-vehicle payload mass capacity and fairing sizes can limit the maximum aperture size, and require more complex deployable structures, as for JWST. Building a larger telescope on the ground may be more cost effective. Ground-based telescopes have already reached 10 m in diameter (i.e., the Keck I and II telescopes). Construction has begun on the ELTs, with diameters ranging from 24.5 to 39 m [5–7], and concepts exist for telescopes approaching 100 m in diameter [8]. Given the relationships for angular resolution and background-limited point-source sensitivity, achieving the diffraction limit on such large telescopes is highly desirable, and solutions have been developed and implemented for countering the effects of atmospheric turbulence using adaptive optics (AO).

AO allows us to recover the diffraction-limited performance of large telescopes on the ground by measuring the degradation of the incoming wave front and correcting the wave front in real time [3,9,10]. After decades of development, AO is now in routine operation at all major large-diameter astronomical observatories [11–18].

Although AO correction is now widely employed in the astronomical community, it is currently an imperfect solution for imaging geosynchronous Earth orbit (GEO) objects. A key drawback is that imaging with AO requires a bright reference star, or guide star, close to the object being studied. In the case of imaging GEO targets, the situation is further complicated by the sidereal motion of GEO objects relative to naturally occurring guide stars (NGSs). One solution to this problem uses lasers projected from the ground up onto the sodium layer of the atmosphere (at altitudes of 80–100 km) to produce an artificial reference source where needed [19–24]. These laser guide stars (LGSs) have significantly improved the "sky coverage" for AO for astronomical imaging, but in turn have drawbacks. A reference source within the atmosphere can be used to sample only a part of the turbulence. In addition, the source itself is an imperfect reference due to having a finite angular size (it is not a point source, for example), and the brightness of the source is limited. Further improvements to the LGS solution are needed to achieve optimal performance on the new ELTs, and this paper addresses these needs by using nanosatellites with onboard lasers pointed at Earth as reference sources that can be placed in desired orbits.

The paper is organized as follows: in Sec. II, we review the fundamental limits of AO performance and some of the potential applications of high-performance AO, which motivated this study; in Sec. III, we present and justify the technical assumptions used throughout the analysis; in Secs. IV and V, we analyze the requirements for satellite orbits to enable observations of both astronomical targets and GEO objects, respectively; in Sec. VI, we analyze the required laser-transmitter power, pointing requirements, beamwidth, and ground spot size; in Sec. VII, we discuss the feasibility of packaging a satellite guide star (SGS) system in a small satellite; finally, we conclude in Sec. VIII with concepts and technologies, which should be developed or further studied to enable SGS systems.

II. Motivation

We begin motivating the use of nanosatellite guide stars by looking at the benefits of augmenting current GEO monitoring strategies with ground-based AO systems. We then describe applications for high-resolution high-Strehl imaging, highlight the fundamental limits of NGS AO performance, and briefly review some of the strategies developed to mitigate these limits.

A. AO for GEO Object Imaging

As the GEO belt becomes increasingly populated and contested, the need for imaging of critical commercial and military systems within the belt has continued to grow [25]. In the following sections, we present the motivation for imaging the GEO belt from Earth using AO and an SGS rather than imaging using satellite-based telescopes and cameras.

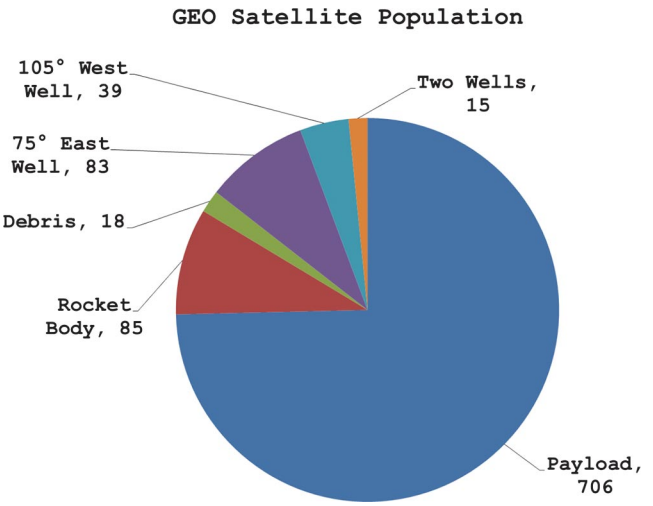

Fig. 1 Graphical breakdown of GEO belt satellite population from analysis of satellites in libration points [27].

Operators began using the GEO belt for Earth observation and communication beginning in the 1960s, and the belt has continued to be populated. The possibilities of collisions within the GEO belt are becoming nonnegligible with the proliferation of active systems and subsequent inactive satellites, rocket bodies, and debris [26], as seen in Fig. 1. Commercial and government agencies rely heavily on the continued performance of active systems within the GEO belt, and it would be useful to have the ability to image active systems for health status, confirm deployments, and to watch for proximity dangers (either orbital debris or small, active threats) [25].

The GEO and near-GEO satellite population, shown in Fig. 2, gives insight into the number of active and retired systems in GEO, GEO supersynchronous, and GEO subsynchronous orbits. Likely active GEO satellites lie within the green outlined area. Objects at or above 15 deg inclination are not considered for these analyses, as they may be inactive systems inclined under the influence of gravitational disturbances with no station keeping [28]. As of a 2016 full space catalog query [29], there are more than 1100 objects for which two-line element (TLE) sets have been generated with semimajor axes within the 35,000–37,000 km altitude range. (GEO altitude is approximately 35,786 km.)

Threats to the active systems in their critical orbits can come from both active and inactive satellites. Active satellites could be those possibly launched for in-GEO operations for a variety of purposes, like imaging, proximity operations, or purposeful conjunctions. This paper does not contain an in-depth analysis of these mission possibilities, but rather proposes methods for greater space situational awareness (SSA) and space domain awareness. Decommissioned or drifting satellites entering and exiting the GEO belt also pose a very real threat. They are naturally accelerated out of their sidereal orbits to the various libration points within the GEO belt and to greater inclinations [28]. Ground-based radar tracking and TLE analysis can give satellite operators warning of possible conjunction events, but real-time imaging of active, high-value assets (HVAs) would give direct observation of near-conjunction events or possible proximity operations of smaller GEO-located satellites.

B. Optical Performance for Imaging GEO Objects

The importance of high-quality imaging of GEO HVAs for spacecraft health and SSA, in addition to the potential use as a photometric calibration target [30], is compelling reasons to revisit the SGS concept as presented here. Although we do not delve into the analysis and simulation of the imagery possible with ground-based assets, previous work from the University of Hawaii and the University of Arizona has been done to examine the utility and

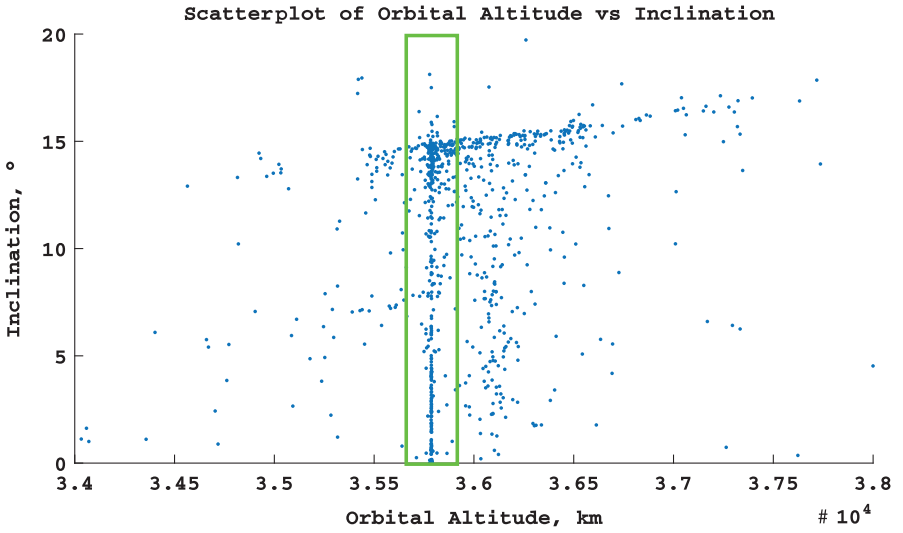

Fig. 2 Scatterplot of GEO belt objects and near-GEO objects; the GEO belt is highlighted in green, with subsynchronous and supersynchronous GEO orbits to the left and right, respectively.

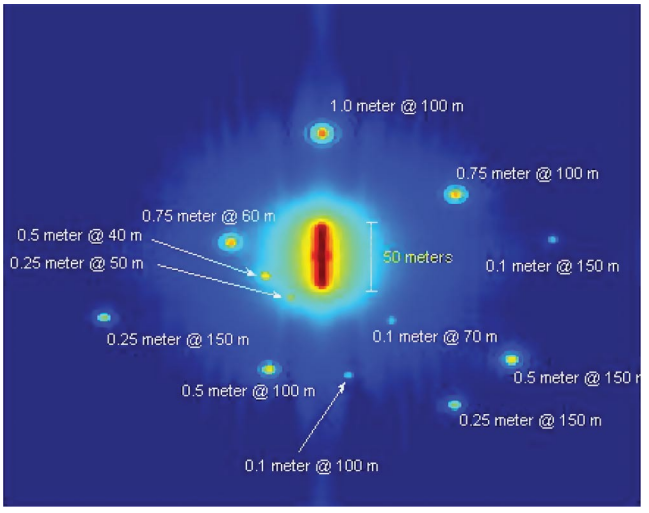

Fig. 3 AO simulated results of the AEOS telescope with a 3 s total observing time; here, the integration times are 384 ms each, at 880 and 440 nm observing wavelengths [31].

feasibility of imaging the GEO belt with ground systems [31]. We present a key figure from their findings in Fig. 3, which shows results from an analysis that studied the Advanced Electro Optical System (AEOS) telescope at Haleakala Observatory in Hawaii. These simulated results are for the 3.65 m system that uses AO to perform image correction and show a simulated scene resolving a main target (ANIK F2, 50×5 m class, mag $+9$) communications satellite clearly distinguished from the surrounding microsatellites. The results appear promising, given the relatively modest telescope size as compared to the next-generation ELTs, along with a total exposure time of 3 s. (We show the possibility of much longer integration times in Sec. V.C.) The results show the target HVA, and nearby microsatellites or orbital debris are clearly distinguishable.

Equally convincing results from the University of Cambridge using ground-based interferometric systems are presented in Fig. 4 using synthetic-aperture interferometric imaging [25]. The panels show a truth satellite image at 1.65 μm of magnitude 8 (left), a reconstructed interferometric image (middle) using capabilities of the Magdalena Ridge Observatory Interferometer, and adding data from an 8-m-class telescope nonredundantly masked to increase image fidelity (right). Here, the wavelength assumed is around 1650 nm, imaging a large GEO satellite spanning 27 m across the solar panels, with exposure times of 1 s. The authors propose using existing telescope systems with nonredundantly masked apertures combined with AO on large-diameter telescopes (8 m for their analysis and simulation). This approach would allow the SSA community to gather high-quality images of the brightest GEO objects using larger, single telescopes to achieve the shorter baselines needed for such an approach. The results presented here show that the target satellite can be seen in detail down to 1.4 m resolution at GEO altitudes. This paper focuses on the feasibility and utility of an SGS system and its application to AO, and does not further investigate the use of interferometric imaging, but both advanced electro-optical imaging and interferometry would benefit from the use of an SGS as a predictable, bright calibration source or artificial guide star.

Direct on-orbit imaging presents challenges for monitoring and diagnosing assets within the GEO belt. Given the volume and size constraints of nanosatellites, as we discuss in this paper, the required aperture for imaging at the visible band ($\lambda = 550$ nm) quickly reaches sizes that present a challenge for these small form-factor buses.

The angular resolution is dictated by the diffraction-limited relationship (known as the Rayleigh limit) between λ and the aperture size D, and is given by

$$\theta \approx 1.22 \frac{\lambda}{D} \tag{1}$$

Further detail about diffraction-limited seeing is presented in Sec. III.A. Because we are considering how well a space-based telescope could do at high-resolution imaging of GEO objects, we can use the diffraction-limited relationship, because the imager will not be affected by atmospheric disturbances. We have chosen a feature resolution of 10 cm to help enable the resolution set as a goal by the 2015 Defense Advanced Research Projects Agency (DARPA) Request for Information on technology solutions for space domain awareness [32]. The distance to a target, d, is needed for determining aperture size. Analyzing the catalog data for satellites that have semimajor axes within a ± 6 km altitude range of GEO altitude, we find a mean orbital distance between 480 (assumed) actively controlled systems within the GEO belt to be $d \approx 550$ km. This active population size agrees closely with the analysis done at the Massachusetts Institute of Technology, Lincoln Laboratory in 2005 [28], and will serve as our assumption for the GEO population for the purposes of determining orbiting imager system parameters. With this d, we can determine the angular diameter of a 10 cm resolved feature of 0.18 μrad. The required aperture diameter for such an on-orbit diffraction-limited GEO-based system would be $D = 3.7$ m (for $\lambda = 550$ nm). A system this size is roughly 150% larger than the

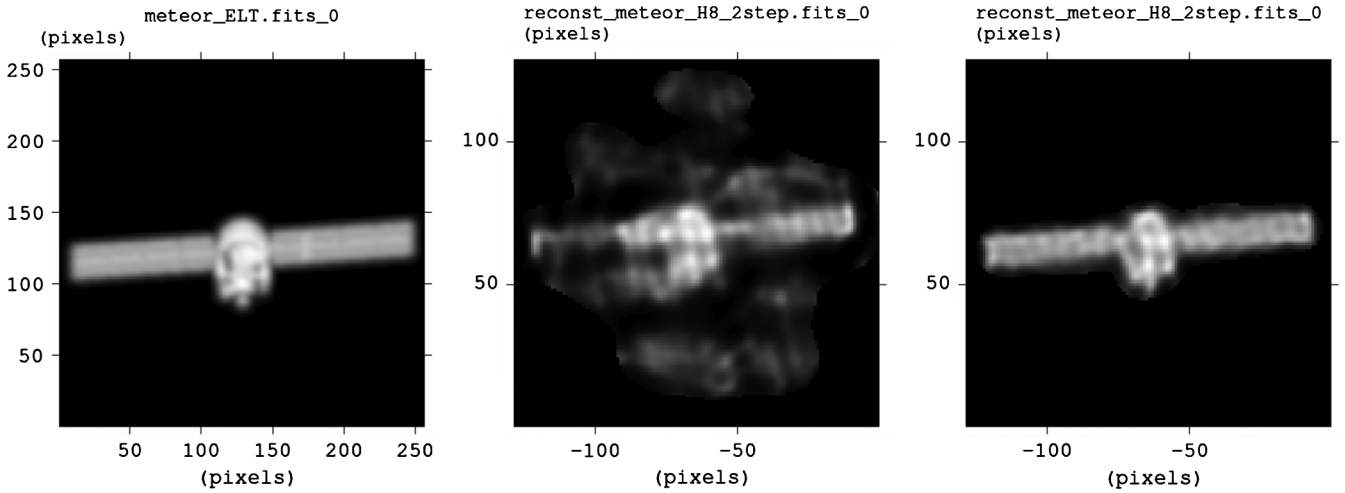

Fig. 4 Interferometric-imaging-simulation results from a bright GEO satellite as the imaging target; the left panel is the truth image, the center is reconstructed using only MROI capabilities, and the right panel shows the addition of nonredundantly masked interferometry [25].

HST. Such a system would require a significant investment given current launch vehicle and fairing sizes, as well as propellant for station keeping and maneuvering.

Alternatively, a system might be designed to fit on a 6U CubeSat ($10 \times 20 \times 30$ cm) that can image to 10 cm feature resolution in space. If we assume that the imaging aperture on such a system is constrained by the smallest dimension of the CubeSat bus, this gives us an aperture of about 10 cm in diameter. Using Eq. (1), we can determine the distance needed to achieve 10 cm linear resolution on GEO targets in the visible band ($\lambda = 550$ nm). Assuming diffraction-limited optics, we find that a CubeSat would need to be within approximately 15 km of the GEO belt altitude. The available volume in such a system would likely be dominated by the optical payload, and would limit the remaining volume to fit a propulsion system (see Sec. VII.B for further discussion of CubeSat propulsion). This leaves the satellite as a largely drifting system, meaning that imaging opportunities would come infrequently, only as often as the satellite passes "below" or "above" the target of interest via circular supersynchronous or subsynchronous orbits. (See Sec. IV for more details of super- or subsynchronous orbits.) The topic of in-space imaging with CubeSats, however, warrants a more detailed discussion and consideration of new technology developments in advanced optics and deployables for CubeSats that are currently beyond the scope of this paper.

We propose an alternative method for observation using ground-based imaging of GEO targets with the use of the large, next-generation astronomical AO telescopes that use SGS systems for their reference sources (See Table 1 for performance metrics.). These proposed approaches could augment or minimize the need for dedicated space-based GEO-imaging satellites. In addition to the use of a dedicated GEO-object-imaging SGS system, in Sec. IV, we consider the feasibility of using a GEO SGS for astronomical-object imaging. We also present the types of ground stations required for reasonable resolutions, and the results of preliminary orbital analyses.

C. Adaptive Optics

AO system designs and implementations vary, but all share a few common components, point-source needs, and inherent limitations. In the following subsections, we give a brief overview of AO and its performance.

1. *AO Performance Limits*

Comprehensive reviews of AO system design and modeling of AO system performance are treated at length in several texts [3,10]. We only focus on a brief high-level description and key points relevant to this work. A depiction of an AO system is shown in Fig. 5. Hardware

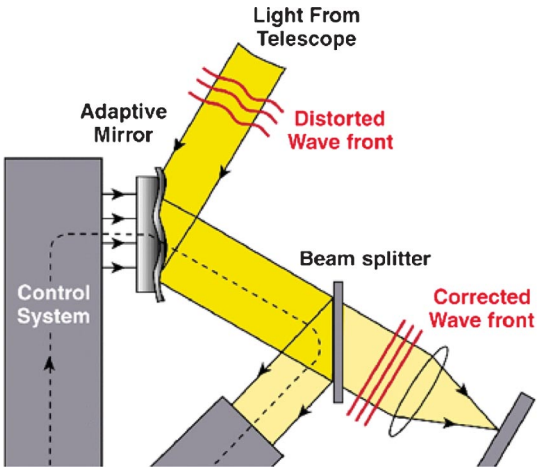

Fig. 5 Depiction of the principles of an AO system; the incoming light is split and sampled to allow for closed-loop control of the adaptive mirror. (Image credit: Claire Max, Center for Adaptive Optics).

components for AO systems include a wave-front sensor (WFS), which measures the degradation of the incoming wave front. (There are different types of WFS, each with their own limits, which we leave to the reader to investigate [33].) These measurements are processed by a real-time computer, which calculates the correction needed. A correcting element, typically a deformable mirror (DM), applies the correction. A key design parameter is the spatial sampling of the WFS and DM (how finely the wave front can be measured and corrected). Any electromechanical system will have a finite response time, and because the turbulence profile is constantly changing, this introduces a temporal error. Given a star of certain brightness, one can divide its light into finite spatial and temporal bins before any measurement is overwhelmed by photon noise. It is this photon noise that prevents the design of an AO system with arbitrarily fine spatial sampling running at arbitrarily high speed.

The key results from an understanding of the limits of AO performance can be summarized as follows:

1) Photon noise places a fundamental limit on AO correction. Even with ideal, noiseless, perfect throughput, an infinitely fast AO system requires a guide star brighter than $V \sim 10$ mag for diffraction-limited imaging in V band. (See Table 2 for photometric letter designations.) As we will discuss in Sec. III, realistic AO systems require even brighter stars.

2) The required spatial sampling is not affected by telescope diameter. Therefore, building larger telescopes does not reduce the impact of photon noise on AO.

Table 1 Rayleigh-limit resolution for ELTs using $\lambda = 550$ nm

Telescope	Diameter, m	Angular resolution	Linear resolution at GEO, cm	Location	Reference
GMT	24.5	0.0056″	98	LCO, Chile	[5]
TMT	30	0.0046″	80	Mauna Kea, Hawaii	[6]
EELT	39	0.0035″	62	Cerro Armazones, Chile	[7]
OWL	100	0.0014″	24	Concept only	[8]

3) There are a limited number of stars bright enough to serve as NGSs. Such stars are not useful as sources for imaging sidereally tracking objects, like GEO HVAs.

2. *Off-Axis Natural Guide Stars*

Natural guide star AO uses a bright star near (off-axis from) the imaging target as the reference. Depending on the separation between the NGS and the target, the AO system measures and attempts to correct turbulence in a column of the atmosphere different from the one through which light from the imaging target propagates. The correction made using the NGS will not be the optimum correction for the imaging target, and this effect is called "anisoplanatism." If the NGS is close enough to the imaging target, useful correction can still be achieved. The area around a star where this is true is referred to as the "isoplanatic patch." (A more rigorous definition of the isoplanatic patch can be found in Sec. III.C.) From Kolmogorov turbulence theory, the wave-front error (WFE, denoted σ_θ) due to this anisoplanatism is related to the angular separation of the target from the guide star, θ, and the isoplanatic angle, θ_0, defined as the Strehl $= 1/e$ distance by the relationship [3]

$$\sigma_\theta = \frac{\lambda}{2\pi}\left(\frac{\theta}{\theta_0}\right)^{5/6} \tag{2}$$

We relate this to image quality using the Strehl ratio S, which is the ratio of the peak height of the PSF to that of a perfect system. Strehl ratio and WFE are related by the Maréchal approximation [34]:

$$S = \exp\left[-\left(\frac{2\pi}{\lambda}\right)^2 \sigma_\theta^2\right] \tag{3}$$

It is evident that θ_0 is the angle at which Strehl ratio has dropped to $1/e$ of its on-axis value. We note that typical values for θ_0 at astronomical observatories are $\sim 3''$ at 550 nm and perhaps $\sim 15''$ at 2200 nm. For an angular separation of $10''$, and using the typical values of θ_0, we obtain WFEs of approximately 240 and 250 nm, respectively. These relatively small θ_0 values, compared with the availability of bright stars to use as natural guide stars, limit the usefulness of off-axis natural guide stars for increasing sky coverage with AO for desired targets. The use of artificial guide stars can overcome these limitations.

3. *Laser Guide Stars*

One technique that has resulted in significant gains in sky coverage is the use of lasers to produce a reference source. The LGS approach projects a laser up from the observatory into specific regions of the atmosphere, and uses the backscattered light for wave-front sensing. Two sources of backscatter are used: Rayleigh, which uses the phenomenon of Rayleigh scattering from altitudes typically around $\sim$20 km [10], and sodium, which uses the return from a layer of sodium atoms at $\sim$92 km altitude [23].

In terms of image quality, the sodium LGS has the best performance due to the height of the reference spot. The main limitation of LGSs is that they can only sample a cone-shaped portion of the turbulence through which light from the target propagates. This "cone effect" results in a WFE given by [3]

$$\sigma_{\text{cone}} = \left(\frac{D}{d_0}\right)^{5/6} \tag{4}$$

The parameter d_0 depends on the turbulence profile and the beacon height. (Higher is better.) Typical values for sodium LGS at good astronomical sites range from 3 to 5 m in V band, and from 15 to 25 m in K band. (See Table 2 for photometric letter designations.) On current large telescopes, this limits single-laser-beacon Strehl ratios to approximately 1% in the visible. At longer wavelengths, such as K band, things are much better. However, on the coming ELTs, single beacons will suffer a significant cone effect even at K band.

Additional drawbacks stem from the fact that the LGS passes through the turbulent atmosphere before forming the artificial star. One consequence of this is that the LGS spot cannot be used to measure image motion (d/tilt), and so a natural guide star is still needed. This NGS can be much fainter ($m \sim 18$ mag) and somewhat farther from the science target than the isoplanatic patch radius. Still, this need for an NGS near the science target ultimately limits the sky coverage of any LGS system.

In addition, traversing the atmospheric turbulence twice causes the apparent size of the source to broaden. Wave-front sensing is most sensitive at the diffraction limit, and so the larger size of LGS spots results in a worse-than-optimal correction. Larger spots are brighter (more scattering area), however, and so there is a tradeoff between photon flux and spot size [35].

Finally, only a small fraction of the photons projected into the atmosphere are returned to the telescope. Consequently, high-power lasers are required to form the guide stars. Although there is much ongoing work to optimize return from the sodium layer, there are limits to the amount of return flux related to the density of the layer [35]. A guide-star brightness equivalent to $V = 5.1$ mag has been demonstrated on sky [36], but this is much brighter than is typically achieved [24].

4. *Multiple Guide Stars*

Much of ongoing research in the development of large-telescope AO systems is focused on ways to overcome the cone effect and to broaden the corrected field of view of AO systems. One approach is to use multiple guide stars.

Multiconjugate AO (MCAO) uses multiple reference sources, either stars or lasers [37]. The wave-front measurements are then applied to several DMs, each conjugate to a different height in the atmosphere. In this way, the corrected field of view (FOV) can be significantly broadened, albeit at a lower correction level than is obtained for an on-axis source at infinity. In laser tomographic AO (LTAO), a tomographic-reconstruction algorithm is used to solve for the three-dimensional structure of turbulence in the atmosphere [38]. Laboratory experiments indicate that multiconjugate and laser tomographic AO will be able to provide Strehl ratios of 22–32% in the visible across a $15''$ FOV on a 10 m telescope [39].

Table 2 Photometric letter designations through near infrared

Letter	Midpoint wavelength, nm	FWHM bandwidth, nm
U	365	66
B	445	94
V	551	88
R	658	138
I	806	149
Y	1020	120
J	1220	213
H	1630	307
K	2190	390
L	3450	472

Developments along these lines should be considered in the context of this study. These techniques could be employed with multiple satellite-borne lasers as well, with a potentially better performance.

LGS systems provide significant gains over the seeing limit on large telescopes. With the advent of multiconjucate AO capabilities, these gains can potentially be extended into the visible, and over wider fields. However, these are complex systems, and given the limitations, such as not being a point source, they are unlikely to achieve as high of a Strehl as desired for diffraction-limited GEO or astronomical-object imaging.

5. Satellite Guide Stars

The concept for an SGS was originally proposed by Greenaway [40] and Greenaway and Clark [41], in addition to proposals to use satellite laser sources as photometric calibration targets [30], and a satellite-based approach has many potential benefits over an LGS system, especially if the cost of the satellite and access to space is reduced. The laser does not need to scatter (either Rayleigh backscatter or scatter from the high-altitude sodium layer as in LGS systems) with returned power high enough to generate a detectable reference source. A system that uses a satellite-based laser projected downward with a narrow beamwidth can use a low-power laser, even if it is at a larger distance (as is shown in Sec. VI). An SGS will also be well above all atmospheric turbulence, and will provide a small angular-size reference source. A satellite-based LGS can overcome the cone effect and the need for a tip/tilt guide star, and provide a very high photon flux to the WFS. This was the motivation for the proposal for a high angular resolution optical survey (PHAROS) concept [40,41]. Until recently, launching a system like this into space was as complex, if not more so than ground-based LGS systems, and launch costs were prohibitive.

However, in recent years, there has been a paradigm shift to smaller, less expensive satellites [42]. Miniature, common form-factor satellites, called CubeSats, have emerged over the past decade, enabling quick access to space at a fraction of the cost. The small $10 \times 10 \times 10$ cm cube (1U CubeSat) offers a common bus size that allows for easy integration as an auxiliary payload on traditional satellite launches via the standard Poly-Picosatellite Orbital Deployer, and the more recent Canisterized Satellite Dispenser [43] or others. This has enabled rapid technology testing on-orbit and mission concept development. The standardization of small ride-share spacecraft has spurred the miniaturization of the needed subsystem electronics, optics, attitude control, communication, power, propulsion, etc., which are now available commercially "off the shelf" (COTS) for CubeSats. This revolution in small-satellite technology motivates us to revisit the SGS system on a small-satellite platform, such as a 6U CubeSat, measuring $10 \times 20 \times 30$ cm and typically with mass of $\leq$14 kg.

III. Design-Study Assumptions

In the following sections, we discuss the design for the proposed CubeSat platform. Although our design would work for a number of different wavelengths for the laser, and in fact could support multiple different lasers, we initially use 850 nm and provide rationale for that selection. For light-pollution reasons, it is very important to emphasize that the laser would normally be off, and only commanded on when ground-based observations were desired, and when on, has an extremely narrow beamwidth. The effects of the beamwidth on ground spot size are discussed in Sec. VI.B.

A. Resolution

The angular-resolution limit of an imaging system is set by diffraction, as seen in Eq. (1). An imaging system has a PSF that is the modulus squared of the two-dimensional Fourier transform of the aperture. For an unobstructed circular aperture, this is the well-known Airy pattern. A common definition of angular resolution is the Rayleigh criterion, which states that two point sources are resolved when the Airy peak of one coincides with the first null of the second's PSF. As mentioned earlier, this occurs when the sources are separated by approximately $1.22\,\lambda/D$. We note that, for a centrally obscured aperture, as in a telescope with a secondary mirror, the multiplicative factor is smaller than 1.22 by 10–20% in typical configurations. There are also other definitions (for instance, the Sparrow criterion), which adjust the amount of overlap between the PSFs. For simplicity in this study, we use the Rayleigh criterion.

We can infer the ability of the ELTs with AO to image GEO objects by considering their ability to resolve features or objects at GEO altitudes. Using Eq. (1), we obtain the results in Table 1 for the upper limits for angular resolution and corresponding linear resolution metrics at GEO altitudes for the different ELTs, assuming their performance is meeting the Rayleigh criterion. We consider the Giant Magellan Telescope (GMT), the Thirty Meter Telescope (TMT), the European Extremely Large Telescope (EELT), and the Overwhelmingly Large Telescope (OWL).

B. Choice of Wavelength and Brightness Goal

It is desirable to have the SGS transmit at wavelengths that are not visible or harmful to the human eye (the maximum-permissible-exposure level for a 10 s exposure is about 100 $\mathrm{mW/cm^2}$ for a 1550 nm laser [44]), and for which we can use inexpensive detectors that do not require complex system support, such as cooling. It is also beneficial if the wavelengths are selected, such that the transmitter is power efficient and can close a link from GEO with sufficient margin, as presented in Sec. VI.

Several considerations drive our choice of wavelength for the SGS beacon. Current AO systems most often use silicon-based detectors in the WFS, and so designing for existing systems implies a wavelength $\lambda < 1000$ nm. In Fig. 6, we show the bandpass for the Magellan AO (MagAO) system WFS [18,45]. MagAO is mounted on the 6.5 m Magellan Clay telescope at the Las Campanas Observatory (LCO). Its WFS has a central wavelength of 780 nm and peak sensitivity around 850 nm.

In addition to MagAO, other current-generation AO systems, such as the Large Binocular Telescope AO (MagAO is essentially a clone of the Large Binocular Telescope [17]) and the Gemini Planet Imager, have WFSs that work at about *I* band as well. Table 2 serves as a reference for the photometric letter designations.

We use MagAO to establish the SGS minimum photon-flux requirement. MagAO is noteworthy because it delivers Strehl ratios greater than 40% in the optical ($\lambda < 1000$ nm) on bright NGSs [46]. In Fig. 7, we illustrate this capability, showing WFE vs NGS brightness in the WFS bandpass. The dotted lines are predictions from detailed analytic-performance modeling. The asterisks are on-sky measurements at various wavelengths, and the red curve and points correspond to good (~25%) conditions, blue corresponds to median conditions, and black to poor (~75%). It is clear that a star brighter than ~8 magnitude is required for optimum performance. There is a sharp drop in performance (increasing WFE) starting at $m \sim 8$ magnitude.

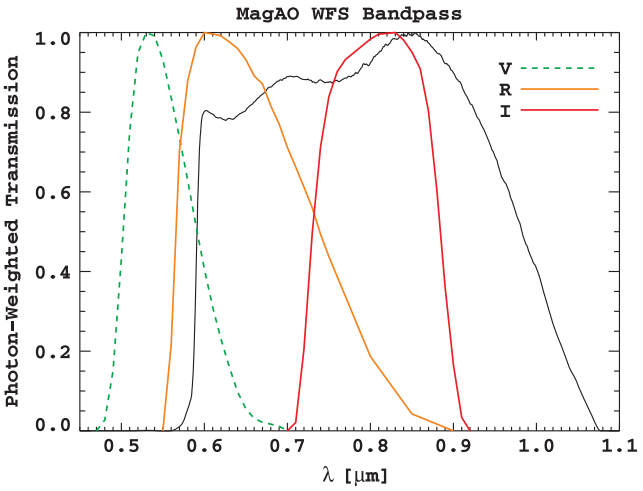

Fig. 6 WFS bandpass curve (solid black curve) for the MagAO system [45]; the peak sensitivity is in the near infrared.

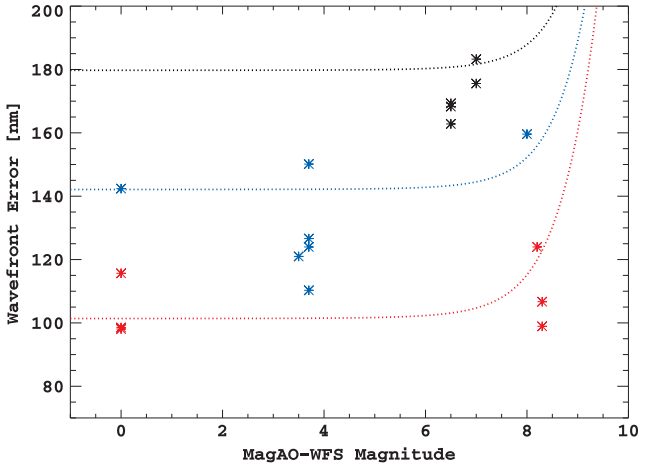

Fig. 7 MagAO performance vs guide-star magnitude; on-sky points are from the MagAO visible AO CCD (VisAO) camera. (Figure adapted from [47]).

Integrated over the spectrum of Vega in the MagAO WFS bandpass [45], which is centered at 0.78 μm, a zero-magnitude star has a flux of $F_{\text{ref}} = 5 \times 10^9$ photons/m^2/s [48]. Therefore, to achieve an $m \sim 8$ magnitude star or brighter, using Eq. (5), the minimum photon-flux requirement for the system is $F = 3.15 \times 10^6$ photons/m^2/s. We use this in Sec. VI for the analysis of proposed laser systems on the satellite.

$$m - m_{\text{ref}} = -2.5\log_{10}\left(\frac{F}{F_{\text{ref}}}\right) \tag{5}$$

C. Isoplanatic Patch

The isoplanatic "patch" is the column of atmosphere through which the telescope is observing where disturbance qualities can be approximated as temporally coherent, and where the turbulence pattern is statistically similar. It is defined as θ_0, and it is related to Fried's parameter r_0 and the FWHM of the system. The isoplanatic patch translates the Fried parameter to an angular distance from the optical boresight. Here, we also take into account the LCO FWHM seeing value (denoted $\text{FWHM}_{500\text{nm}}$ at the center wavelength of 500 nm denoted λ_{LCO}) and the zenith angle θ_z [10]. The proposed SGS has a center wavelength of 850 nm (denoted λ_{desired}); thus, we correct for this from the LCO center wavelength. This results in the relationship [2]

$$r_0 \approx 0.98 \times 0.206265 \times \left(\frac{\lambda_{\text{LCO}}}{\text{FWHM}_{500\text{nm}}}\right)\left(\frac{\lambda_{\text{desired}}}{\lambda_{\text{LCO}}}\right)^{6/5} \sec(\theta_z)^{-3/5} \tag{6}$$

which yields $r_0 \approx 29$ cm for the 850 nm SGS. We next examine at the turbulence height of our imaging system.

The turbulence characteristic height for AO systems is important to capture, as it allows us to complete the calculation of the isoplanatic patch. The turbulence characteristic height is dependent upon the AO ground site chosen; it is a function of the site altitude above sea level. Using a standard height assumption of 5 km [49], we can determine a characteristic height for analysis. Because the altitude above sea level of the LCO site is 2400 m, we subtract that from the 5000 m standard height assumption and use $H = 2600$ m. With this, we obtain an isoplanatic patch half-angle from the equation:

$$\theta_0 \approx 0.314\frac{r_0}{H} \tag{7}$$

which yields approximately $7.3''$ for the angular radius of the isoplanatic patch at a wavelength of 500 nm.

D. Telescope Pointing Angle

Telescope tracking away from zenith also has an effect on the isoplanatic angle. Here, θ_z is defined as the angular deviation from zenith, such that $\theta_z = 0$ deg corresponds to pointing straight upward from the local horizontal. As the ground system tracks the SGS in its orbit, θ_z increases and incident light must travel through more of the atmospheric turbulence layer. The effective isoplanatic angle decreases to account for this. This is captured in the secant term in Eq. (6) for r_0 in Sec. III.C. Figure 8 shows the effects of θ_z on the isoplanatic patch size. Greenaway proposes a 45 deg angle limit (red dashed line) to avoid a costly decrease in the isoplanatic patch angle θ_0, as the SGS line of sight deviates away from the observing telescope zenith line [40]. At this proposed limit, θ_0 has decreased by nearly 20% to only $6''$. A hard limit (brown dashed line) is presented at 10 deg elevation ($\theta_z = 80$ deg) for typical real-world horizon limits, with elevation limits being more restrictive for the ELT systems.

E. Orbit Considerations

Besides pointing angles, each AO ground system will have a given altitude below which a guide-star system will not project its source fully through the appropriate volume of atmosphere; a projection of the telescope aperture will be larger than the isoplanatic patch. We must determine this minimum orbital altitude for such systems. For LCO, with an aperture diameter of 24.5 m and the previously calculated nominal isoplanatic half-angle of approximately 7.3 arcsec, we should take into account the cone effect when determining the minimum altitude alt_{min}. The WFE due to the cone effect is described in Sec. II.C.5. A simplified expression for the "effective diameter" d_0 [10] is

$$d_0 \approx 0.90\frac{r_0}{H}\text{alt}_{\text{SGS}} \tag{8}$$

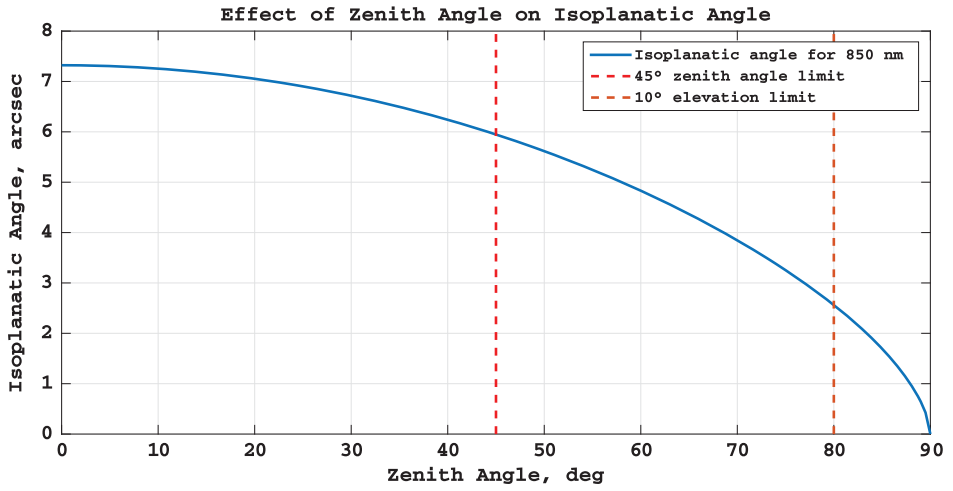

Fig. 8 Plot of zenith-angle effect θ_z on the isoplanatic patch angle; the dashed line shows a 45 deg angle limit proposed by Greenaway [40], due to the extreme limiting effects on θ_0 beyond 45 deg.

This is conservative, as it includes piston and tilt terms in the approximation. We choose to design the system to have at most a 1% Strehl ratio impact from the cone effect, that is, $S_{\text{cone}} = 0.99$. We then have

$$\text{alt}_{\text{min}} = \frac{1}{0.90[-\ell_n(0.99)]^{3/5}} \frac{DH}{r_0} \tag{9}$$

or

$$\text{alt}_{\text{min}} = 17.6 \frac{DH}{r_0} \tag{10}$$

For GMT having parameters $D = 24.5$ m and $H = 2600$ m, we get $\text{alt}_{\text{min}} \approx 6600$ km km.

F. Effect Compared to Observational Overheads

Typical observatory overheads in setting up a new observation include slewing the telescope, tracking the dome, and fine-tuning the acquisition of the science target on the optical axis. AO overheads add setting AO parameters and closing the loop. AO overheads at Keck Observatory in LGS mode, for example, are 7–13 min [50]. However, the contribution of the telescope and AO overheads would not have an effect on the total integration time if the SGS is placed so as to account for these acquisition and loop-closing times, by placing the SGS within the isoplanatic patch of the science target after typical observatory overheads have passed.

We next examine candidate orbits and architectures for the SGS mission, from the highly elliptical solutions proposed in earlier literature by Greenaway and Clark to using an SGS system in a geosynchronous orbit [41].

IV. Orbit Analysis for Potential Astronomical Imaging

A. Astronomical Observation Orbits

Although not the primary focus of this paper, we consider the ability of using these systems for imaging astronomical targets of interest, as the scientific community would benefit from the use of the SGS as well. Because of the relatively small scale of the isoplanatic patch, SGS systems will require a new operational approach to maintain usability for targets of interest. The satellite is only a useful reference source for AO when its light falls within the isoplanatic patch (although it still has value as a photometric calibration target outside of this separation). A major challenge in designing an LGS mission is that, for many orbits, the alignment between the target and guide stars happens infrequently and for a relatively short duration compared to the orbital period.

B. Astronomical Reference Targets

For the sake of the following analysis, we chose the Hubble Deep Field (HDF) and Hubble Ultra Deep Field (HUDF) as astronomical targets. These are of interest for placeholder analysis in that they represent fields intentionally chosen by the original mission to not have bright stars to allow long exposures by HST. This makes them challenging targets for ground-based diffraction-limited imaging.

C. Integration-Time Analysis

For the astronomical observation orbits, we follow Greenaway's [40] approach. Greenaway proposed an intuitive method to design the orbit to maximize the integration time [40]. Highly elliptical orbits (HEOs) were used to match the satellite's apogee velocity to the observatory velocity due to Earth rotation without using propulsion. In addition, Greenaway set the apogee velocity slightly slower than the observatory velocity, and apogee position slightly higher than the declination (DEC) of the target, so that the satellite executes a tight loop around it in apparent motion. The same approach is also used in this study. Figure 9 shows sample trajectories of SGSs for a target whose DEC angle is 5 deg, observed by the TMT. Here, the imaging target for the TMT is assumed to be located at (0, 0) in right ascension (RA) and DEC.

To increase the integration time, the obvious adjustment is to increase the orbital altitude. However, because the altitude for a

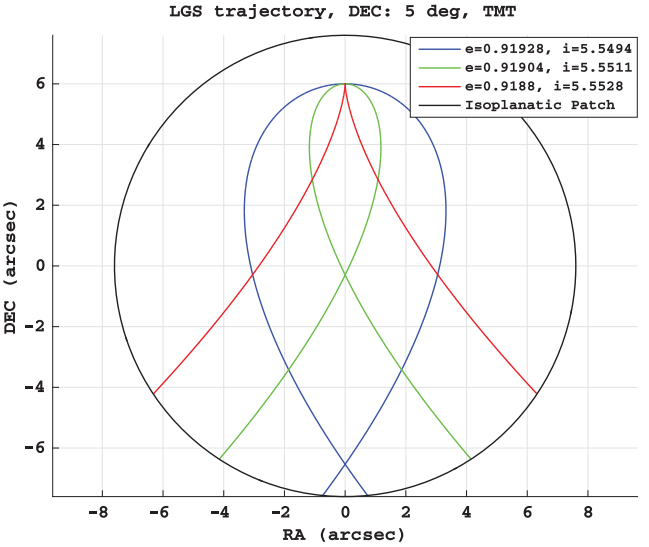

Fig. 9 SGS trajectory within an isoplanatic patch with a radius of 8 arcsec (black outer circle); the different color curves show the differences present in only minor eccentricity and inclination changes.

system that assumes no onboard propellant is directly related to the launch cost, it is impractical to do so without bounds. The maximum characteristic energy (C_3) that a launch vehicle can impart is predetermined (dependent on the launch vehicle), and the orbital period is identical for different orbits with the same C_3. For this study, we will assume orbits with a five-day period whose C_3 is -3.22 km^2/s^2 as was used in Greenaway and Clark's work (chosen because, when the satellite is at or near apoapsis, it can remain within 1.5 arcsec of a target for over 5000 s) [41]. The isoplanatic patch angle of 7.3″ is used (calculated in Sec. III.C). For the following analysis, simple two-body Keplerian orbits are assumed, ignoring other perturbations, such as third-body gravitational effects, asymmetric gravitational potential of Earth, or atmospheric drag. Finally, the GMT and TMT are assumed as the ground observatories.

The integration times available for the ground stations to view the targets (HDF and HUDF) depend highly on the DEC angle of the target. Figure 10 shows the maximum integration times for the two observatories vs the target DEC. We show that the integration time exponentially decreases as the target's DEC increases.

For the targets of interest, the maximum integration time vs the orbital period is calculated and shown in Fig. 11. As shown in the plot, and as intuitively expected, the integration time increases with longer orbital periods. However, as the orbital period increases, the number of opportunities for AO observations decreases proportional to the orbital period: we have only one AO opportunity per orbit. To maintain

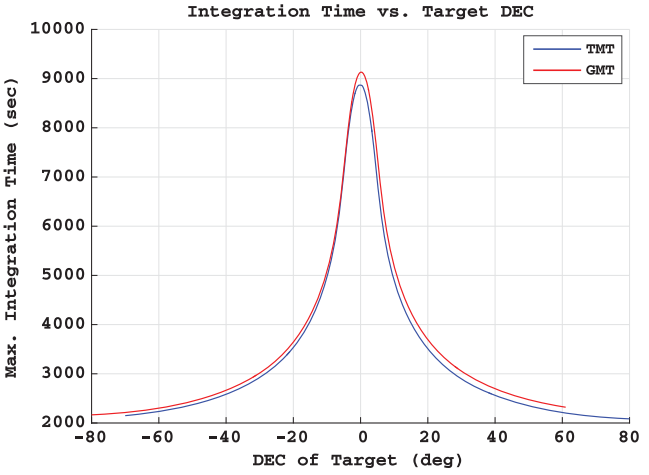

Fig. 10 Maximum integration times depending on DEC of targets for 5-day-period orbits; curves shown are for the TMT and GMT.

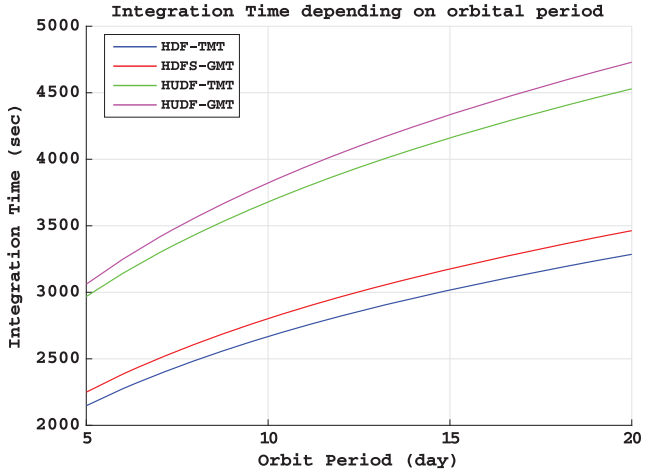

Fig. 11 Maximum integration times depending on orbital period are shown for different Hubble targets as examples; the RA and DEC of the Hubble targets are given in Table 3.

continuous coverage, there would have to be multiple satellites in orbit spaced one observation period apart. For a five-day orbit (432,000 s) with 5000-s-long observation windows, this would require an impractically large constellation of 87 satellites. We present these high-level findings here, and note that a more detailed trade between orbit geometry, integration time, constellation size, and the number of AO observations would be of interest for future work.

D. Analysis for Maneuvering for Astronomical Targets

Analyzing orbital periods and target DEC gives us insight to only a portion of the complexities of using SGS for astronomy. In this section, we also analyze the energy cost to change the spacecraft velocity for accessing orbits for different targets. This would allow the use of a single SGS for multiple astronomical targets. This cost is typically reported as delta V (or ΔV, in kilometers per second) [51]. A straightforward approach has been used to calculate ΔV, and the results do not guarantee optimality. The objective of this section was to give a reference ΔV for the orbit maneuvers.

The orbit maneuvers consist of two parts: 1) orbital plane change with a single impulse and 2) coplanar transfer with a single impulse. The objective of the maneuvers was to transfer between orbits that allow a single SGS to be used for different astronomical targets. Table 4 shows the required ΔV to transfer between the two orbits. Here, ΔV_p is defined as the delta V for part 1, and ΔV_c is defined as the delta V for part 2. ΔV_{total} is then the combined cost, or $\Delta V_p + \Delta V_c$. All orbital periods are assumed as 5 days identically, and the sequence of orbital events can be either plane change first or coplanar transfer first, which impacts the results of ΔV_{total}. Here, we show that ΔV_{total} ranges from 4 to 8 km/s, all of which would be too large for onboard thrusters on nanosatellite platforms to achieve in a reasonably short period of time for the current technology. Even though high-efficiency electric propulsion could achieve the total required delta V for one such maneuver, its low thrust would require a maneuver time longer than one year. This initial analysis makes it clear that each astronomical target would require a dedicated satellite, whereas a single satellite can support an observation of multiple GEO targets.

E. Comparison to Visible LTAO

The concept that is most comparable to an SGS-based system in the context of scientific observations is LTAO, which we briefly introduced in Sec. II.C.4. Laboratory results presented by Ammons et al. [39] show that a five-laser LTAO system on a 10 m telescope could provide 22–32% Strehl across a 15″ field of regard. Such an LTAO system requires at least five high-power lasers [39], and likely more for a larger-aperture ELT.

For comparison, consider that a well-optimized AO system could deliver on-axis Strehl as high as 80% in the visible (at $H\alpha$, [47]) with a bright guide star, and that an SGS operating within our assumed isoplanatic angle of 7.3″ will maintain Strehl $> 1/e \times 80\% = 29\%$. So the SGS would provide at least as good image quality, albeit over a smaller field. A more comprehensive system comparison would require developing an end-to-end simulation of an observing campaign with each system, and a costing exercise for each. As astronomical observations are not our main focus here, we defer a comprehensive comparison of an SGS system to an ELT-scale LTAO system to future work.

V. GEO Observation Analysis

We next examine the use of a space-based 850 nm LGS system with a ground telescope capable of a full isoplanatic patch angle of approximately 15 arcsec ($2\theta_0$), as presented in Sec. III.

A. Elliptical Orbits

We first consider the highly elliptical Greenaway-type [40] orbit to see if GEO imaging is possible using SGSs that are intended for astronomical targets, as seen in the previous section. However, elliptical orbits are useful for matching the sidereal rate of the stars at apogee relative to the AO system, rather than matching GEO orbital velocity. Performing orbital analysis with Analytical Graphics, Inc. Systems Tool Kit (STK) [52], we find that there exist few and very-short-duration GEO imaging opportunities with an elliptical orbit. Only for short time frames (on the order of 10 s maximum) does the SGS approximately match GEO rates. A simulation of a year-long mission (October 2014 to October 2015) shows integration times total only about 3000 s using two-body Keplerian modeling. Including higher-order orbital perturbations due to the gravitational harmonics or three-body dynamics quickly reduces the integration times by up to two orders of magnitude, achieving less than 30 s over the year. We note that, for the STK simulation, it is assumed that a satellite in an HEO cannot change its orbital parameters. The ΔV required to adjust such a high-energy orbit would likely not be cost effective.

Having demonstrated that HEOs are not a good match for regular GEO imaging, we next examine using an SGS within the GEO belt. An SGS could act as a resident space object for one satellite being imaged, or more than one satellite if propulsion requirements are small. In Sec. VII.B, we estimate that a 6U CubeSat can reasonably

Table 4 ΔV for orbital maneuver[a]

Orbit transfer	ΔV_p, km/s	ΔV_c, km/s	ΔV_{total}, km/s
HDF — HDFS	0.23	7.17	7.40
HDF — HUDF	3.52	4.77	8.29
HDGS — HUDF	0.41	3.62	4.03

[a]See Table 3 for RA and DEC of the Hubble target fields.

Table 3 Integration time for targets of interest

Target	(RA, DEC)	Observatory (latitude)	Integration time, s		
			5 days	10 days	20 days
HDF	($12^h36^m49.4^s$, +62° 12′58″)	TMT (19°49′58″N)	2462	3059	3768
HDFS	($22^h32^m56.2^s$, −60° 33′02″)	GMT (29°01′42″S)	2579	3213	3972
HUDF	($3^h32^m39.0^s$, −27° 47′29″)	TMT (19°49′58″N)	3404	4219	5195
HUDF	($3^h32^m39.0^s$, −27° 47′29″)	GMT (29°01′42″S)	3510	4383	5424

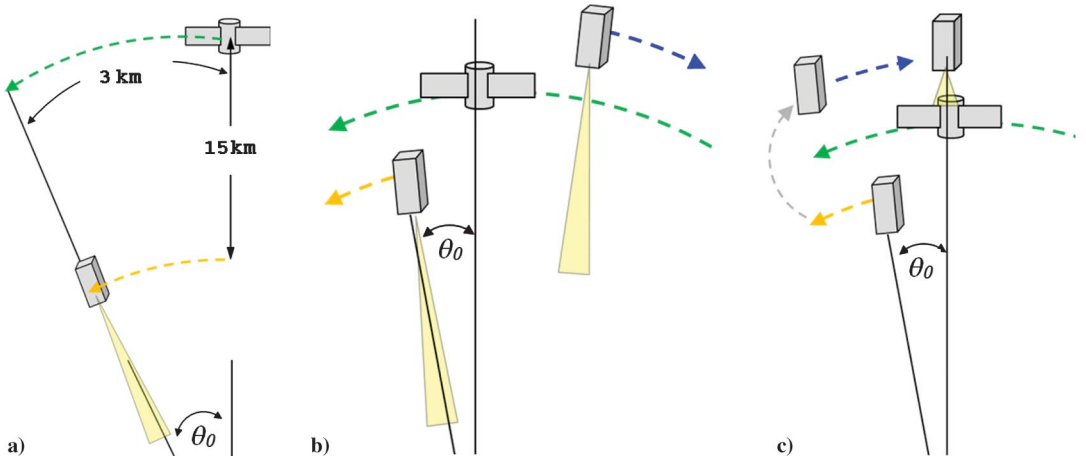

Fig. 12 GEO-based SGS with a) relative distances to a potential imaging target, b) the imaging target with subsynchronous and supersynchronous guide stars above and below, and c) revisiting the imaging target with a change in altitude.

carry 2 kg of fuel, and still accommodate the guide-star payload and other necessary spacecraft subsystems. This can support longer integration times near target satellites. Figure 12 shows the relative distances of the SGS to the target satellite that it is commanded to share the isoplanatic patch with. The SGS would only turn on its payload when in view of and needed by ground stations, and would allow for imaging without needing to illuminate the object of interest. In Sec. V.B, we show only modest ΔV costs to obtain lengthy integration times and to reposition the SGS within the GEO belt. These very low delta V costs assume the satellite can come to arbitrarily close proximity to the target satellite, well within the 500 km separation distance mentioned earlier for in situ imaging

B. Proposed Concepts of Operation

Three main concepts of operations are presented for AO imaging of the GEO belt for space situational awareness or asset health and status assessment: subsynchronous SGS, supersynchronous SGS, and a revisit mission. Subsynchronous GEO satellites are those that have slightly lower altitudes than the GEO altitude of 35,786 km, and thus move at a faster orbital rate than the GEO motion. Objects in these orbits migrate relative to the GEO belt in an eastward direction. Supersynchronous are the converse, having higher altitudes and moving relative to the belt in a westward motion. Diagrams of the supersynchronous and subsynchronous orbits relative to a standard GEO satellite are shown in Fig. 12b, upper, lower, and middle orbits, respectively.

We propose that SGS operators would be able to control the relative rate at which the satellite passes above or below a target, thus controlling the integration time for the system. For lengthy integrations, operators would be able to move into proximity of a target system and match the sidereal rate to allow for indefinite imaging. Figure 12a shows the maximum in-plane distances that a GEO SGS system should maintain to fall within the same isoplanatic patch as the target satellite. The diagram presents a subsynchronous example. Finally, a coorbital revisiting mission is presented in Fig. 12c. Here, the subsynchronous guide star allows imaging during a fast, lower-altitude pass, but can raise altitude to allow for a secondary integration opportunity of the same target.

C. GEO SGS Delta V Analysis

Here, we discuss the mission-design impact for executing the different scenarios in terms of delta V. The costs for executing these imaging maneuvers are fairly modest as compared to those presented for the astronomical targets in Sec. IV.A. These costs are shown in Fig. 13 for a single imaging event with variable integration times. It can be seen that, as the desired integration times increase, the cost to change from a standard GEO altitude decreases. Figure 13 shows the continuum of delta V costs for only 1.2 s of integration time and their associated orbital altitudes. The integration time here refers to the total available time that the SGS is within the isoplanatic patch with the target satellite.

In considering these missions, we must also look at the requirement to maintain a safe distance from the imaging target or other GEO objects. Avoiding an SGS-caused conjunction with the satellite of interest is extremely important. Because the guide-star satellite would be moving in the GEO belt relative to the target, it is critical to keep track of its position. For example, when the integration times reach greater than approximately 14 h, the guide-star-satellite orbital radius falls within 500 m of the target satellite (for both sub- and supersynchronous orbits). For lengthy integration times, a stop-and-perch approach might work best, but would require more propellant to enable. This could be accomplished by approaching the target satellite and matching orbital speeds to reside in near orbit until the imaging is complete, as seen in the concept of operations (CONOPS) in Sec. V.B. Once finished with imaging a target, the SGS could then be commanded to move to other longitudes of the GEO belt.

A GEO-based guide-star satellite with propulsion has the flexibility of repositioning within the orbital belt. Here, only in-plane equatorial maneuvers are proposed, in an effort to keep maneuvers within the capabilities of a CubeSat. The results of the delta V analysis are presented in Fig. 14, showing the delta V costs associated with moving the guide-star satellite up to 10° in longitude eastward (subsynchronous) or westward (supersynchronous) relative to an arbitrary geostationary point using a transfer ellipse and recircularization into GEO. Only two-body mechanics are assumed, along with impulsive maneuvering. For missions in which traversal time is not an issue, a 10° longitude change can be accomplished for less than 10 m/s in delta V for a 30-day transfer time. Figure 14 presents the lower bound as a 24 h transfer time. Subsynchronous (eastward) and supersynchronous (westward) transfers are presented for the bounding cases (for this paper) of 1 and 10° longitude changes over 1- through 30-day transfer times. The ΔV costs include speed changes into transfer ellipses and recircularization into GEO orbits.

Further mission analysis reveals that these are not the only delta V costs that a GEO SGS would need to account for. GEO north–south station keeping is on the order of several longitude maneuvers per year. Solar and lunar third-body effects contribute approximately 50 m/s/year of delta V that must be consumed to maintain a 0 deg inclination [51]. Uncorrected, the spacecraft inclination would drift from 0 to 15 deg at the GEO belt. These effects can be seen in the scatterplot of the GEO belt population, in Fig. 2. Decommission or uncontrolled satellites are naturally accelerated into the higher inclinations over several decades [51].

We have shown that a GEO-based guide-star satellite can be useful to greater science community, as well as for potential commercial- or government-related tasking. These artificial guide-star systems can act as repositionable calibration sources for different ground systems with relatively small delta V costs. They can serve for AO imaging of

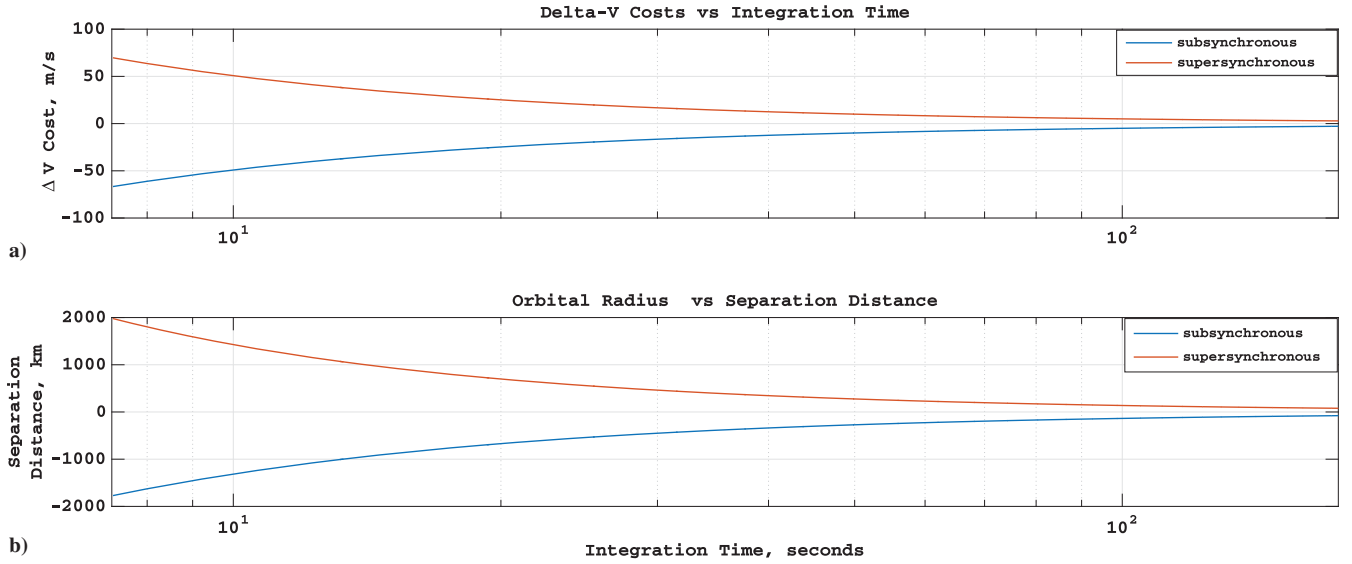

Fig. 13 Plotted are a) the delta *V* costs for respective integration times (seconds along the *X* axis) and b) the orbital-radius difference between the SGS and the imaging target satellite.

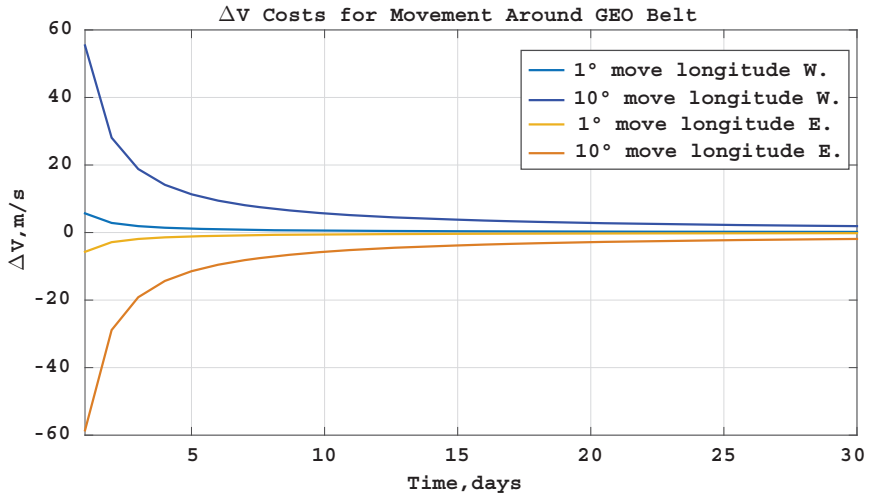

Fig. 14 Delta *V* costs associated with longitude changes within GEO; these delta *V* costs would be added to any mission-related burns for station keeping.

the GEO belt for HVA monitoring and space situational awareness assessments. In Sec. VI, we discuss the enabling technology needed for such systems, the laser payloads, the satellite bus, propulsion system, and the attitude dynamics and control system.

VI. LGS Payload Design

The laser-payload design is driven by 1) the need to emulate the brightness of a star and 2) the ability to direct light efficiently toward ground telescopes, ideally with little spillover. This must be accomplished within the constraints of the pointing and attitude-determination-and-control-system (ADCS) capabilities. In this section, we discuss the requirements for the SGS system to satisfy the imaging requirements determined for astronomical and GEO object observing (Secs. IV and V, respectively). We also consider the impact on pointing and ADCS design of the SGS system.

To use the laser payload as a guide star, the laser must appear no dimmer than an $m \sim 8$ magnitude star, giving a required minimum photon-flux requirement for the system of $F = 3.15 \times 10^6$ photons/m^2/s, as discussed in Sec. III. To achieve this photon flux to the ground, we first establish the pointing accuracy for the satellite. Considering the beamwidth of the laser transmitter (with margin), we calculate the ground spot size necessary for achieving the desired minimum photon flux. We also account for beam divergence and aperture size for the system. We check to ensure the laser transmit power required from the CubeSat is reasonable for a continuous imaging interval (assuming no duty cycling for this analysis).

We use this analysis to evaluate whether or not the requirements for the SGS pointing system are practical for a low-cost 6U CubeSat, and to make design modifications, if necessary, within the power budget.

A. Laser-Transmitter Beamwidth, Pointing Accuracy, and Ground Spot Diameter

The beamwidth of the laser transmitter dictates the ground spot size of the laser. Typically, the 3-sigma pointing of the laser [by the spacecraft body itself, or by other pointing stages on the spacecraft, such as a gimbal or fast steering mirror (FSM)] should be one-tenth of the beamwidth [53], meaning that the center of the beam can be placed within $\pm 1/10$ of the beam footprint diameter of the target pointing. We examine the pointing accuracies for state-of-the-art CubeSat control systems, and determine the ground spot diameter for the orbits discussed in Table 5. The authors recognize that contributing factors, like pointing stability and wheel-induced jitter, orbit-determination (OD) accuracy, and timing accuracy, must also be considered in future work, although they are not used in this preliminary feasibility analysis. Another important aspect to consider is atmospheric broadening of the beam due to scintillation and other atmospheric effects [30].

Table 5 For imaging an eighth-magnitude LGS, the following table presents the required photon rate to emulate an eighth-magnitude star and the laser-transmitter power required to generate the necessary photon flux on the ground[a]

Imaging parameters	Pointing accuracy		
	GEO: 35,786 km		
Pointing accuracy	30″	60″	0.5°
Ground spot diameter, km	52.05	104.1	3,131
Required photon rate, photons/s	6.712×10^{15}	2.685×10^{16}	2.429×10^{19}
Transmitter power, W	0.0026	0.0105	9.460
	HEO: 100,000 km		
Pointing accuracy	30″	60″	0.5°
Ground spot diameter, km	145.4	290.9	8,749
Required photon rate, photons/s	5.242×10^{16}	2.097×10^{17}	1.897×10^{20}
Transmitter power, W	0.0204	0.0817	73.87
	HEO: 400,000 km		
Pointing accuracy	30″	60″	0.5°
Ground spot diameter, km	581.8	1164	35,000
Required photon rate, photons/s	8.386×10^{17}	3.355×10^{18}	3.035×10^{21}
Transmitter power, W	0.327	1.307	1,182

[a]For pointing accuracies of 30″, 60″, and 0.5°, the parameters are calculated parameters for GEO and HEO orbits.

We consider a spread of three possible pointing accuracies for low-cost nanosatellites (e.g., 6U CubeSats) available today. As a reference, the BRIght Target Explorer satellites have demonstrated less than 45 arcsec (3σ) pointing performance on nanosatellite buses using Dynacon reaction wheels and a star tracker [54]. The Optical Communications and Sensor Demonstration satellites from The Aerospace Corporation state they expect to demonstrate better than 0.1 deg using custom components designed and built by The Aerospace Corporation [55]. Both examples have more advanced ADCS systems than typical low-cost technology-demonstration CubeSat programs would. (We discuss this further in Sec. VII.A.)

Using the pointing accuracy ($3-\sigma$) multiplied by a factor of 10 as the beamwidth ϕ, the ground spot diameter D_{spot} is determined by multiplying the tangent of the beamwidth by the orbit altitude h:

$$D_{\text{spot}} = 2h \tan\left(\frac{\phi}{2}\right) \tag{11}$$

This calculation assumes a 0 deg inclination orbit for a ground station located at the equator. The ground spot diameter as a function of orbit altitude can be found in Fig. 15, and the values for the GEO and HEOs can be found in Table 5.

We also consider the beam divergence of the laser transmitter. Beam divergence is inversely proportional to the aperture size, which is limited by the small-satellite size. For an aperture diameter of 2–10 cm, the beam divergence is approximately 5.6 to 1.13″ (0.17–0.034 mrad). This beam divergence is small compared to the overall beamwidth. Therefore, the aperture size is not the limiting parameter of the system. More details are provided in Appendix A.

B. Laser-Transmitter Output Power

Using the required minimum photon-flux requirement, as discussed previously and in Sec. III, we find the photon rate (photons per second) required, which drives the power requirements for the laser transmitter. To find the required transmitter power, we multiply the photon rate by the energy of a photon:

$$E_{\text{photon}} = \frac{hc}{\lambda} \tag{12}$$

We take into account atmospheric transmittance losses of 40% for the wavelength of interest [53]. Using an 850 nm laser transmitter (see Design-Study Assumptions in Sec. III), the required laser-transmitter power is listed in Table 5.

For an SGS in GEO, the transmitter output power must be roughly 2 mW, 11 mW, and 9.5 W for 30″, 60″, and 0.5 deg (0.914, 1.82, and 54.8 mrad) pointing accuracies, respectively (assuming a factor of 10 spread in the beamwidth, which is typically specified to minimize the signal loss caused by pointing errors [53]). Figure 16 shows the transmitter power necessary as a function of orbit altitude for the three pointing accuracies. For a small-satellite system, it is reasonable to provide up to 10 W of electrical power to the payload for an extended period of time, and the electrical-power-to-optical-power conversion efficiency can be baselined at about 10% efficient [53], although it may be a bit higher. Therefore, for an SGS in HEO, pointing accuracies would likely need to be around 60″ (1.82 mrad), as an input power of 10 times the transmit power required for 0.5 deg pointing is too high. Section VII contains further discussion of the satellite design and feasibility.

C. Laser-Payload Requirements and Hardware Solutions

The laser payload will be made from COTS fiber-optic telecommunications components. Depending on the required optical power, the 850 nm laser light could be generated either by a high-power laser diode (HPLD) or by a low-power seed laser and optical amplifier. The light would travel along fiber-optic cabling and be sampled, to monitor output power and beam quality, before reaching the collimator. The laser beam then leaves the collimator and, if the spacecraft can achieve the desired pointing of about 60″ (1.82 mrad) with a star tracker and reaction wheels, exits a transmit aperture. If the spacecraft body is not able to achieve the desired pointing, or if additional disturbances are likely, or if the ground spot size and power are to be minimized, after the beam exits the collimator, it could bounce off an FSM or a miniature gimbal before leaving the spacecraft, similar to the AO system on the NASA Laser Communications Relay Demonstration project [56].

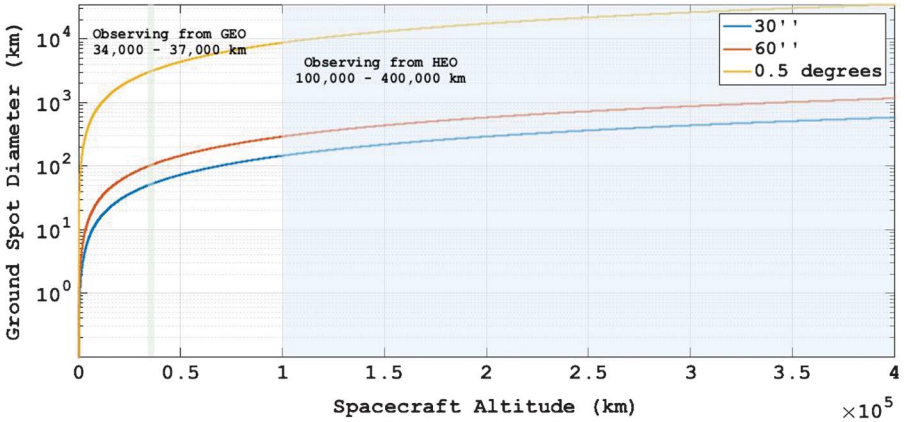

Fig. 15 For a given spacecraft orbit altitude, ground spot diameters are plotted for 30″, 60″, and 0.5 deg $3-\sigma$ pointing accuracies; tighter (smaller) pointing accuracies and lower altitudes yield smaller ground spot sizes.

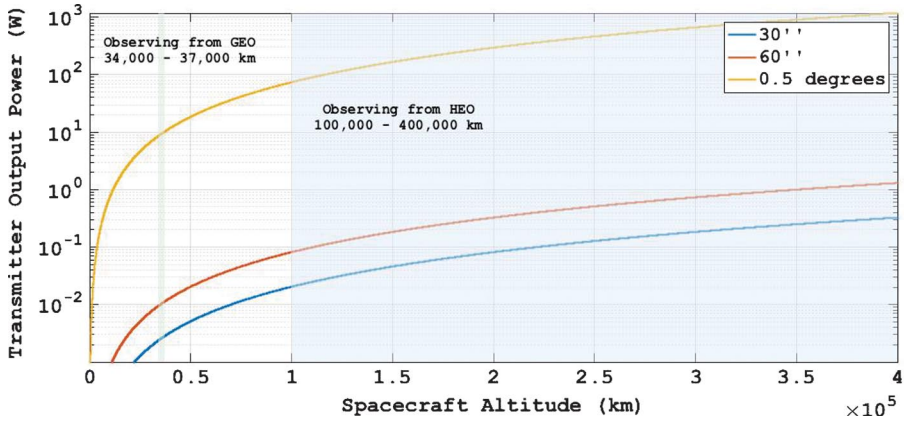

Fig. 16 For a given spacecraft orbit altitude, laser-transmitter output powers are plotted for 30″, 60″, and 0.5 deg 3 – σ pointing accuracies; tighter (smaller) pointing accuracies and lower altitudes yield less required power.

Fiber-coupled laser diodes (850 nm) are available with optical output power on the order of 100 mW. This approach has the advantage that it is cheaper and simpler to implement, while having greater overall electrical-to-optical-conversion efficiency. The 100 mW of optical power would be sufficient for many of the GEO and low-altitude HEO operations described in Sec. VI.B, but would be not bright enough for use in the higher-altitude HEO orbit (requiring up to 100 W), or if the pointing requirements were relaxed ($> 60''$).

1. *Master-Oscillator-Power-Amplifier Configuration*

If greater optical power is required, the transmitter can be constructed in a master-oscillator-power-amplifier (MOPA) configuration, wherein a low-power diode laser produces a modulated laser signal, which is then fed into an optical amplifier. The optical amplifier would likely use a tapered amplifier chip with a tuned output wavelength centered on 850 nm. Once the signal has been amplified, it is carried by fiber-optic cable to a collimator.

All of the components required for a MOPA laser system are commercially available, and can all fit within a 1U form factor, with a mass less than 1 kg. The 850 nm seed laser diode can be purchased off the shelf from commercial suppliers, but would need special packaging (for sealing and venting) to survive launch and operate in the space environment. A commercially available optical amplifier specifically for an 850 nm laser, which yields an output optical power of 1 W and could be used on a 6U CubeSat, weighs approximately 30 g and is less than 0.1 U in volume [57].

2. *Nonlinear Optics for Frequency Doubling*

Another optical technology that may be beneficial for SGS is nonlinear optics for frequency doubling (also known as second-harmonic generation) [58]. A nonlinear optical crystal, made of materials, such as periodically poled lithium niobate (PPLN) [59], could be used to convert 850 nm light into 425 nm. This would allow the same laser system to drive a second band for less than the mass cost of an entire second laser. In this respect, the application would be similar to that of the MOPA architecture.

SHG is sensitive to the polarization of incoming light. The conversion efficiency of a PPLN crystal is also sensitive to the poling period being matched to the wavelength being doubled, which can be controlled by modulating the temperature of the crystal. Both of these can be used to control the frequency-doubling process, allowing either the original or second harmonic to be produced on command [59].

Nonlinear crystals do not perform SHG with 100% efficiency, and as input power increases, higher harmonics are also generated. For some applications, such as green laser pointers [60], the unconverted input light and parasitic higher harmonics are filtered, but these may actually be beneficial for SGS, so that multiple bands can be excited simultaneously; I and B for the case of 850/425 nm, or H, I, and V if a COTS 1550 nm laser (widely available from the fiber-optic communications industry) are driven with enough power to produce doubling to 775 nm and third-harmonic generation at 517 nm.

To produce longer wavelengths, nonlinear optics can also be used for difference-frequency generation in optical parametric oscillators (OPOs). OPOs can be very broadly tunable, with ranges of several hundred or even thousand nanometers, but require an additional optical cavity, which may not be feasible in a CubeSat form factor [61].

VII. SGS Bus Requirements and Hardware Solutions for a 6U CubeSat

The preliminary system-design constraints for an SGS can all be met on a small spacecraft using existing technologies. We examined the laser system in Sec. VI.C, which would be the payload on the spacecraft, and we discuss the key spacecraft bus subsystems in this section. We focus on the CubeSat form factor, as CubeSat platforms allow for quicker, less expensive access to space. Compared with its 1U and 3U counterparts, the 6U CubeSat allows for increased capability, such as propulsion and power generation, while maintaining a spacecraft size that still has containerized deployers available for hosted ride shares to orbit.

Given the modular and standardized design of CubeSats and CubeSat deployers [62,63], the size, weight, and power requirements and constraints for the spacecraft are stringent. The volume restrictions for the spacecraft are set by the deployer, and the mass restrictions on the CubeSat form factor have been standardized in the California Polytechnic State University CubeSat Design Specification [63]. For a 6U CubeSat, the size is restricted to approximately $10 \times 20 \times 30$ cm, and the spacecraft mass must not exceed 14 kg [62]. For power requirements, the limitations stem from both the available surface area on which to place solar cells, as well as available mass and volume in which to store secondary batteries. To provide additional power beyond the limitations of body-mounted solar panels, we use a single-deployed single-sided solar panel with the dimensions of 20×30 cm along with body-mounted panels. Such a power system can nominally supply orbit average power up to approximately 50 W. (See Appendix B for a more detailed calculations of the power supplied.)

The following sections describe the enabling technologies and components for the proposed 6U design for the satellite LGS, referencing both the NASA Ames Research Center report on "Small Spacecraft Technology State of the Art," [64] as well as the authors' experience. Because of the higher risk posture and lower cost of many CubeSat programs, the technical maturity of many of the components is not as high as would be expected of typical space-flight programs. NASA has developed a method of gauging the readiness of technologies based on different parameters. Technologies are given a rating from 1 to 9 on the technology-readiness-level (TRL) rating system. A TRL rating of 1 is the lowest, in which a technology idea is being researched. A TRL rating of 9 shows that a technology has passed all validation hurdles and has completed successful flight

mission operations. For the subsystems we present in the following sections, many of the enabling technologies are relatively immature with limited or no flight heritage, and have TRLs in the 4–6 range.

A. Guidance, Navigation, and Control

Guidance, navigation, and control (GNC) includes both the components used for OD and the components for ADCSs. The driving factors of the GNC requirements are the laser beamwidth and the altitude, because the overall goal of GNC is to point the laser beam to the observatory on the ground. The requirements for OD and ADCS are therefore strongly related to each other. Table 5 gives the GNC requirement baseline for three different orbit scenarios. If assuming $60''$ pointing accuracy for ADCS, the onboard OD requirement should be half of the ground spot diameter, which is 52 km for GEO. For the GEO application, onboard Global Positioning System receivers cannot reliably be used for OD [65]. Communications systems that include ranging capability, as well as OD using the laser transmitter, can augment ground-based radar-tracking systems. (A discussion of laser-transmitter pulse and timing characteristics for this application is an item for future work.) For most space objects, it is possible to obtain TLEs [66], ephemerides published by the U.S. Air Force and made available through the website Space-Track [67]. TLEs used with an orbit propagator, such as a simplified general perturbations model [68], can be used to estimate the spacecraft's position. For attitude determination, sensors, such as star trackers, sun sensors, Earth sensors, gyroscopes, accelerometers, and magnetometers, can be used to determine pointing direction. For control, actuators, such as reaction wheels, thrusters, and magnetic torque rods, have been miniaturized for CubeSats, although the weaker magnetic-field strength at GEO compared with low Earth orbit (LEO) limits the utility of magnetic torque rods. CubeSat propulsion systems are discussed further in Sec. VII.B.

To achieve the relatively high-accuracy pointing (for CubeSats) required in (Sec. VI) likely requires the use of miniaturized star trackers. State-of-the-art star trackers for small spacecraft claim up to 25 arcsec of pointing knowledge and have a TRL of 9 [64]. In addition to individual components, there are also commercially available integrated attitude determination and control units that combine three reaction wheels, a three-axis magnetometer, a star tracker, and three magnetic torque rods, and are designed to provide pointing accuracy of 0.007 deg (1 sigma), or $25.2''$ (0.77 mrad) [69–71]. The integrated ADCS units are generally less than 0.5 U in volume, less than 1 kg in mass, and consume about 5 W when fully active [69–71].

B. Propulsion

In this section, we consider propulsion options to achieve the delta V required for the GEO orbit maneuvering discussed in Sec. V.C. We compare the following propulsion solutions in Table 6: electrospray ("iEPS"), cold gas, ion, and green monopropellant ("green MP"). Hydrazine propulsion systems for CubeSats exist, but hydrazine is more hazardous to personnel and spacecraft than green monopropellant, and so launch service providers are more reluctant to carry secondary payloads with hydrazine.

Green monopropellant has the obvious advantage of having far greater instantaneous thrust, which allows orbital maneuvers to be performed quickly while minimizing the required delta V. The previous orbital-maneuvering calculations used the assumption of impulsive maneuvering (see Sec. IV). This advantage in instantaneous thrust must be weighed against the higher specific impulse of the electrospray and ion-thruster technologies, which allows a spacecraft to obtain a higher useful delta V for a particular unit mass of propellant expended. The cold-gas thruster, while possessing moderate instantaneous thrust and very low specific impulse, is simpler and has more extensive flight heritage and a higher TRL level [64]. A further consideration relates to the electrical power consumed during thruster operation; the ion-thruster technology would likely need to be duty cycled in operation due to the relatively significant power draw associated with continuous operation. Additionally, thermal management may be a concern for some of the described thruster technologies, which is an item for investigation in future work.

In the end, the radio-frequency (RF) ion thruster's high specific impulse and high fuel capacity give it the highest delta V capacity of all of the systems (2300 m/s in a 14 kg 6U CubeSat). This is enough delta V to complete a transfer from geostationary transfer orbit (GTO) to GEO (which requires 1600 m/s if performed from an equatorial launch; 2 km/s if performed from a 30 deg inclined orbit from, e.g., the NASA Kennedy Space Center), and still have 300–700 m/s leftover, enough for dozens if not hundreds of longitude-change maneuvers. The orbit-raising maneuver will have serious practical implications for the mission, as achieving a total impulse of 1500 m/s on a 1.15 mN thruster would require nearly 150 days of continuous firing, and even longer when taking into account duty cycling and the fact that the spacecraft will only be firing when it is near apoapsis. However, none of the other systems provide enough delta V to go from GTO to GEO, and so a spacecraft using any of those systems would need to be carried by a host spacecraft all the way to GEO, which would substantially increase the mission cost (and likely delay launch).

Once the spacecraft reaches GEO, the low thrust of an ion thruster has much less of an impact on mission operations. To transfer 10° east or west in 15 days, the spacecraft would need to execute maneuvers with a total of 3.8 m/s of delta V This would require 15 h of firing at maximum thrust, which would be doubled in practice to accommodate duty cycling, but that would still be much less than the overall maneuver time.

However, while an ion thruster would have ample propellant and delta V capacity to perform the mission studied here, the months-long transfer from GTO to GEO will increase the spacecraft's exposure to radiation. Therefore, whereas most of this analysis focuses on the one-year mission in GEO proper, the power-system sizing in Appendix B assumes a total system lifetime of two years.

C. Power

The power system must be able to generate, regulate, store, and distribute power to all systems, including the laser-transmitter payload at about 10 W, as described in Sec. VI. Assuming a rough power requirement of at least 20 W (10 W for the laser transmitter, ~4 W for ADCS during laser pointing, and 6 W for the other systems), commercially available deployable CubeSat solar panels and batteries are sufficient. This can be achieved with solar panels as a primary power source and batteries as the secondary power source (when the panels are not generating power). The solar panels would

Table 6 Current thruster technologies suitable for small spacecraft and their propulsion capabilities and parameters[a]

Thruster technology	Propellant	Thrust, mN	ISP, s	Electrical power, W	Fuel capacity	TRL
iEPS (2x Busek BET-1mN) [72]	Ionic liquid	1.4	800	30	150 g	5
iEPS (2x Accion TILE) [73]	Ionic Liquid	3	1800	50	400 g	5
Cold gas (2x Vacco MiPS) [74]	Cold Gas	20	40	20	1.2 kg	7–8
Ion (Busek BIT-3) [75,76]	Iodine	1.15	2100	75	1.5 kg	5
Green MP (Busek) [77]	AF-M315E	500	220	<15	2 kg	5

[a]The TRL is also provided. Thrusters marked "2x" are intended for use in a 3U CubeSat, and so a 6U would use two of them, and so thrust, power, and fuel capacity are doubled.

include both deployable and body-mounted panels for peak power needs (particularly if green monopropellant or electrospray thrusters are selected for the propulsion system). See Appendix B for an initial calculation of the power generation from the solar arrays and the energy-storage capacity of the batteries for this application.

D. Structures and Thermal Control

Using an off-the-shelf CubeSat structure can simplify the satellite-development process and can facilitate integration with a standardized dispenser. Off-the-shelf 6U structural components and primary structures (chassis) are offered through several companies [78,79]. Most are machined from 6061-T6 or 7071 aluminum, and are designed with several mounting locations to provide configuration flexibility [64].

The aluminum structure will also serve as a key component in the thermal subsystem, in which it will help to conduct away heat from key components and serve as a thermal mass to minimize the effect of transient perturbations to the spacecraft's thermal environment. The thermal-control system needs to manage the operating modes, duration, and power dissipation of each of all components and subsystems. For GEO and HEO spacecraft, the spacecraft will receive constant sunlight for the majority of the year.

For power-generation reasons, the exterior of the spacecraft, which doubles as the thermal-control surface, will likely be covered almost completely with solar cells. Although solar cells have an intentionally high absorptivity, they also have a high emissivity. Therefore, solar cells act as efficient radiators of heat, and a dedicated radiator is likely not needed. Because all of the exterior surfaces radiate heat effectively, care can be taken to choose whether to thermally couple or decouple components to or from the spacecraft walls. For example, the high-power dissipating laser-transmitter hardware can be coupled to the wall using thermally conductive gap filler. Conversely, batteries, which dissipate only a marginal amount of heat and do not operate well while cold, can be intentionally thermally decoupled from the wall to make sure they stay within operating temperature ranges. The placement of components inside the spacecraft can also be incorporated in the thermal design, and simple resistive heaters can be used where necessary. The thermal design does not require much size or weight. Thermal-control components, like thermal straps, are likely not necessary, which can be verified with a detailed thermal analysis.

E. Command and Data Handling

The command and data handling (C&DH) can be done with the use of COTS avionics hardware along with custom flight software. CubeSat avionics vary in complexity and processing power, but typically rely on the use of a single motherboard in the avionics system architecture. Given the volume constraints of these spacecraft, the use of interface boards can be used to minimize the volume needed for wiring for data and power, and maximizing the utility of the volume used. Interface boards typically connect C&DH with each of the major subsystems, like the ADCS and propulsion, and often include power-distribution units for components.

With the variety of components (sensors, actuators, microcontrollers, or microprocessors) active on such systems, the use of multiple types of command protocols is needed. Protocols often seen in CubeSat components are RS-232, RS-422, I^2 C, and serial peripheral interface (SPI). (This is a nonexhaustive list.) Data storage and transmission for systems, like an SGS, would be minimal, because these are not science-focused missions with data-heavy payloads. The majority of data would be housekeeping and telemetry data, and could easily be accommodated on solid-state flash storage available for CubeSat motherboard hardware.

Several software platforms exist to expedite the process of developing flight software. These platforms serve as middleware between different software modules, and control how data move within the satellite's C&DH system. Currently available platforms include NASA Goddard Space Flight Center's Core Flight System [80] and the Space Dynamics Laboratory and the U.S. Air Force Research Laboratory's SPA Services Manager (in which SPA is Space Plug-and-Play Avionics) platform [81], both of which are available in at least partially open-source implementations.

F. Communications

Uplink and downlink communications can be handled with a bidirectional RF system. The RF system would be used for telemetry, command, and navigation. The RF system should support ranging, a feature that is not yet common in CubeSat transceivers. CubeSats operating in LEO have traditionally used low-power vhf and uhf radios and simple monopole antennas. Because received power decreases as the square of the transmission distance, more sophisticated communications architectures may need to be adopted for GEO and HEO orbits. RF transceivers for CubeSats are commercially available, which operate at higher frequencies, including in the S (2–4 GHz), C (4–8 GHz), and X (8–12 GHz) bands. For the purposes of operating these RF communications systems, an Federal Communications Commission radio service license would be required. A detailed table of the communications systems on currently deployed CubeSats is provided in Klofas [82].

Using higher frequencies makes it possible to realize higher antenna gains both on the ground and on the spacecraft. Vhf and uhf spacecraft radios typically use a quarter-wave monopole antenna with an isotropic gain of around 2.15 dBi [83]. It is not practical to use higher-gain antenna designs (such as microstrip patch antennas) for most vhf and uhf frequencies, as these designs are too large to fit on CubeSats. For higher frequencies, the required dimensions of high-gain designs become smaller, allowing them to be used on CubeSats. Higher-frequency patch antennas are increasingly becoming commercially available, and can occupy just under 1 U of surface area with gains on the order of 8 dBi [84]. For even higher frequencies, such as those in the X band, patch-antenna arrays with up to 16 dBi gain are available [85].

The RF ground station is just as important as the transceiver in closing a link budget, especially to GEO. Past amateur satellite missions operating on vhf and uhf frequencies have used simple ground-station antennas, such as Yagi antennas. This arrangement is cheap and easy to implement, but performance is limited. Uhf operates at 0.3–1 GHz. A lower frequency (compared to S- or X-band downlinks) results in a larger 3 dB beamwidth (and therefore, lower gain), and so more receiving-antenna collecting area is needed. In addition, ionospheric effects are proportional to $\sim 1/f^2$. Better-funded missions may have the option of using established ground stations, such as those available at NASA's Wallops Flight Facility or commercially available ground stations. NASA Wallops Flight Facility hosts both uhf and S-band receive dishes with gain-to-noise temperature (G/T) of 10.6 and 23 dB/K, respectively [86]. X-band downlink is available through facilities at the Poker Flat Research Range and others with G/T typically exceeding 30 dB/K [87].

G. Launch Opportunities

Although more challenging than securing a launch opportunity to LEO, a 6U CubeSat to GEO is possible, given the frequency of launches to GEO. Launch opportunities for CubeSats typically come as auxiliary payloads on rockets with already-manifested primary payload satellites. For a 6U SGS with a desired GEO orbit, the SGS would likely need to share a ride with something, like a GEO communications satellite. GEO communications satellites comprise roughly one-third of recent launches (24 launches of 73 total launches in 2014 [88]). For example, Spaceflight coordinates commercially available rides to GTO for 6U CubeSats starting in 2018 for a relatively modest $1M [89].

VIII. Conclusions

After assessing the laser payload needed for an SGS mission, and the maneuverability that would be desired to enable a mission to visit multiple targets, the authors investigated whether a 6U CubeSat with currently available COTS systems, or combinations of custom and COTS solutions, could meet these mission needs. Laser-payload optical components are commercially available that would satisfy the

mission requirements of 10 W input electrical power (with up to at least 20 W), with about 1 W of output optical power. The current state of the art in CubeSat and small-satellite ADCS should support the required 60″ (1.82 mrad) fine-pointing capability on a 6U CubeSat platform.

This study shows that the SGS concept appears to be viable in the context of a CubeSat mission. Providing a bright ($< \sim 8$ magnitude) reference source for AO at arbitrary positions on the sky would enable diffraction-limited observations with large telescopes on any target. Using only natural guide stars, such observations are limited to $< 0.01\%$ of the sky. With LGS, the need for a tip/tilt guide star limits such observations to $< \sim 10\%$ and generally requires observations at longer wavelengths for true diffraction-limited imaging. In contrast, the SGS concept enables observations of essentially any part of the sky at the diffraction limit, provided an SGS constellation is created and maintained for the desired portion of the sky. Here, the authors have shown that this flexibility in observing also includes the GEO belt and is more feasible in comparison with astronomical applications. With the coming 24–39 m ELTs, this translates to submeter-scale resolution on GEO objects. Used with long baseline interferometers, an SGS will help enable the 10 cm resolution at GEO set as a goal by DARPA.

There are several key technical trade studies that will be needed in preparation for an SGS mission, specifically relating to the design of the laser-transmitter payload, the spacecraft's ADCS system, and the means of propulsion. As identified in this work, both HPLD and MOPA architectures are possibilities for generating the required laser light. The HPLD architecture has the advantage of being simpler, lighter, and more power efficient, whereas the MOPA architecture has the advantage of being very easily scaled to larger optical transmit powers. This trade is partially dependent on the required laser pulse and timing characteristics, the choice of the optical transmit wavelength to be used, and whether or not any nonlinear optical elements will be implemented to achieve frequency doubling.

A more comprehensive analysis of the spacecraft's navigation and ADCS system must be performed. For the initial feasibility analysis on this system, factors, like pointing stability and wheel-induced jitter, OD accuracy, and timing accuracy, were ignored, but must be considered in future work. Although these effects may put an upper bound on the maximum achievable performance of the SGS, they are not expected and substantially affect the baseline feasibility analysis performed here.

The trade study on which propulsion system to implement must also be revisited as new technologies become available. For a sample CONOPS to image 10 separate target satellites in one year, the authors estimate that it would take 87 m/s of delta V, including 3.8 m/s delta V to navigate from a GEO drop-off location that is 10° in longitude away from the first desired target in 15 days. Assuming longitude changes of 10° east or west between targets and a 20-day transfer time, this mission plan would enable approximately 150 days of potential imaging time across the 10 targets. Although the authors' baseline analysis concluded that a green monopropellant system best fits this need due to its high specific impulse (ISP) and high thrust, with further development, another solution may prove superior and allow a longer mission and more sophisticated maneuvers. This trade would also require further consideration of thermal effects depending on how much heat the thruster rejects to the spacecraft. Propulsion that enables CubeSats to maneuver with significant amounts of delta V within relatively short timescales is a key area for further technology development and demonstration.

Several remaining mission or CONOPS trades exist as well. Although this paper focuses on the feasibility and utility of an SGS system applied to AO, it does not cover applications of the SGS system as a photometric calibration source. In this role, the SGS system could potentially be of great value in interferometric imaging and advanced electro-optical imaging. Whether or not using the SGS in this application would place any constraints on it, primary AO mission has not been considered here and would require additional analysis.

Additionally, the trade between integration time, the frequency of opportunities for AO observations, and number of satellites must be considered. It is generally desirable to have longer integration times. This would be achieved by placing the spacecraft in a higher orbit with a longer orbital period, which unfortunately decreases the number of opportunities for AO observations in a manner that is proportional to the orbital period. This is due to the limitation of only having one opportunity per orbit. Because of the low-cost nature of CubeSats, it may be possible to deploy a constellation of SGSs, which would allow multiple observations per orbital period. The operational considerations of utilizing such a constellation have not been investigated here, but the concept is worthy of further investigation.

Appendix A: Laser Beam Divergence and Aperture Size

For the required photon flux to the ground, we analyze the beam divergence of the laser and the aperture size. The beam divergence is inversely proportional to the aperture size. For a small satellite, the aperture size is a constraint and is often limited by the satellite size. Therefore, we examine the beam divergence and aperture size. Assuming a diffraction-limited system, the beam divergence φ is given by

$$\varphi = \frac{2\lambda}{\pi w} \tag{A1}$$

in which w is the beam waist (radius of beam at narrowest point), and λ is the laser wavelength. For an aperture diameter of 2–10 cm, the beam divergence is approximately 5.6–1.13″. This beam divergence is small compared to the overall beamwidth. This range of aperture diameters can be accommodated on a 6U platform. The aperture size is not the limiting parameter for the system.

Appendix B: Solar-Panel Power Production

The approximate power generation of the 6U CubeSat is calculated assuming body-mounted solar panels on five sides (assuming that the equivalent area for cutouts, the laser aperture, etc., is roughly one 2×3 U face). For the five sides, the active area is

$$\begin{aligned} A &\approx (30 \times 20\ \text{cm}) + 2 \times (30 \times 10\ \text{cm}) + 2 \times (20 \times 10\ \text{cm}) \\ &\approx 0.22\ \text{m}^2 \end{aligned}$$

Assuming a 70% solar-cell packing efficiency (and considering the area used for hinges, rails, thermal knife drivers, sensors, etc.) [51], the effective area of the solar arrays is 0.154 m^2. The power produced by the arrays is the power at the end of life P_{EOL} multiplied with the effective array area, where the power at the end of life is the power at the beginning of life P_{BOL} multiplied by the degradation. We assume a two-year mission duration ($L = 2$, one year to transfer from GTO to GEO, and one year for science operations) and a degradation of 2% per year ($D = 0.02$). The power at the beginning of life is the product of the solar average power flux, which we assume is 1367 W/m^2 at Earth. Multiplying beginning of life power by the cell conversion efficiency, (assumed to be 28% for multijunction cells), the inherent degradation (assumed to be 75%), and a cosine loss due to the angle of the solar arrays to the sun (assumed 23.5 deg), we have

$$\begin{aligned} P_{\text{array}} &= A_{\text{array}} \times P_{\text{EOL}} = A_{\text{array}} \times P_{\text{BOL}} \times (1-D)^L \\ &= A_{\text{array}} \times P_0 I_d \cos\theta \times (1-D)^L \\ &= A_{\text{array}} \times \eta_{\text{cell}} (1371\ \text{W/m}^2) I_d \cos\theta \times (1-D)^L \approx 28.3\ \text{W} \end{aligned} \tag{B1}$$

For additional power, a deployable 2×3 U panel (single sided) with solar cells on one face could be added. The array area would increase to approximately 0.198 cm^2 and, using Eq. (B1), yield approximately 38.9 W of power.

Acknowledgments

Weston A. Marlow was supported by the U.S. Air Force under U.S. Air Force contract numbers FA8721-05-C-0002 and/or FA8702-15-D-0001. Any opinions, findings, and conclusions or recommendations expressed in this material are those of the author(s), and do not necessarily reflect the views of the U.S. Air Force. Jared R. Males was supported under contract with the California Institute of Technology funded by NASA through the Sagan Fellowship Program executed by the NASA Exoplanet Science Institute. Jim Clark was supported by the Massachusetts Institute of Technology's Deshpande Center for Technological Innovation. Hyosang Yoon was supported by the Samsung Scholarship.

References

[1] Els, S., Schöck, M., Bustos, E., Seguel, J., Vasquez, J., Walker, D., Riddle, R., Skidmore, W., Travouillon, T., and Vogiatzis, K., "Four Years of Optical Turbulence Monitoring at the Cerro Tololo Inter-American Observatory (CTIO)," *Publications of the Astronomical Society of the Pacific*, Vol. 121, No. 882, 2009, pp. 922–934. doi:10.1086/605315

[2] Floyd, D. J., Thomas-Osip, J., and Prieto, G., "Seeing, Wind, and Outer Scale Effects on Image Quality at the Magellan Telescopes," *Publications of the Astronomical Society of the Pacific*, Vol. 122, No. 892, 2010, pp. 731–742. doi:10.1086/653440

[3] Hardy, J. W., *Adaptive Optics for Astronomical Telescopes*, Oxford Univ. Press, New York, 1998.

[4] Seery, B. D., "The James Webb Space Telescope (JWST): Hubble's Scientific and Technological Successor," *Proceedings of SPIE*, Vol. 4850, IR Space Telescopes and Instruments, March 2003, pp. 170–178.

[5] Bernstein, R. A., McCarthy, P. J., Raybould, K., Bigelow, B. C., Bouchez, A. H., Filgueira, J. M., Jacoby, G., Johns, M., Sawyer, D., and Shectman, S.et al., "Overview and Status of the Giant Magellan Telescope Project," *Proceedings of SPIE*, Vol. 9145, Ground-based and Airborne Telescopes V, July 2014, Paper 91451C.

[6] Nelson, J., and Sanders, G. H., "The Status of the Thirty Meter Telescope Project," *Proceedings of SPIE*, Vol. 7012, International Society for Optical Engineering Paper 70121A-18, Aug. 2008.

[7] Tamai, R., and Spyromilio, J., "European Extremely Large Telescope: Progress Report," *Proceedings of SPIE*, Vol. 4004, Telescope Structures, Enclosures, Controls, Assembly/Integration/Validation, and Commissioning, Aug. 2000, Paper 91451E.

[8] Dierickx, P., and Gilmozzi, R., "Progress of the OWL 100-m Telescope Conceptual Design," *Proceedings of SPIE 4004*, Telescope Structures, Enclosures, Controls, Assembly/Integration/Validation, and Commissioning, Vol. 290, Munich, Germany, Aug. 2000.

[9] Beckers, J. M., "Adaptive Optics for Astronomy: Principles, Performance, and Applications," *Annual Review of Astronomy and Astrophysics*, Vol. 31, No. 1, 1993, pp. 13–62. doi:10.1146/annurev.aa.31.090193.000305

[10] Tyson, R., *Principles of Adaptive Optics*, 3rd ed., Academic Press, Inc., San Diego, CA, Sept. 2010.

[11] Troy, M., Dekany, R. G., Brack, G. L., Oppenheimer, B. R., Bloemhof, E. E., Trinh, T., Dekens, F. G., Shi, F., Hayward, T. L., and Brandl, B. R., "Palomar Adaptive Optics Project: Status and Performance," SPIE, Munich, Germany, March 2000, pp. 31–40.

[12] Wildi, F. P., Brusa, G., Lloyd-Hart, M., Close, L. M., and Riccardi, A., "First Light of the 6.5-m MMT Adaptive Optics System," *Proceedings of SPIE 5169*, Astronomical Adaptive Optics Systems and Applications, San Diego, CA, Dec. 2003.

[13] Herriot, G., Morris, S., Anthony, A., Derdall, D., Duncan, D., Dunn, J., Ebbers, A. W., Fletcher, J. M., Hardy, T., and Leckie, B.et al., "Progress on Altair: The Gemini North Adaptive Optics System," *Proceedings of SPIE 4007*, Vol. 115, Adaptive Optical Systems Technology, Munich, Germany, July 2000.

[14] Wizinowich, P., , Acton, D., Shelton, C., Stomski, P., Gathright, J., Ho, K., Lupton, W., Tsubota, K., Lai, O., and Max, C.et al., "First Light Adaptive Optics Images from the Keck II Telescope: A New Era of High Angular Resolution Imagery," *Publications of the Astronomical Society of the Pacific*, Vol. 112, No. 769, 2000, pp. 315–319. doi:10.1086/pasp.2000.112.issue-769

[15] Rousset, G., , Lacombe, F., Puget, P., Hubin, N. N., Gendron, E., Fusco, T., Arsenault, R., Charton, J., Feautrier, P., and Gigan, P.et al., "NAOS, the First AO System of the VLT: On-Sky Performance," *Proceedings of SPIE*, Vol. 4839, Adaptive Optical System Technologies, 2003, pp. 140–149.

[16] Minowa, Y., , Hayano, Y., Oya, S., Watanabe, M., Hattori, M., Guyon, O., Egner, S., Saito, Y., Ito, M., and Takami, H.et al., "Performance of Subaru adaptive optics system AO188," *Proceedings of SPIE*, Vol. 7736, Adaptive Optics Systems II, July 2010, Paper 77363N. doi:10.1117/12.857818

[17] Esposito, S., Riccardi, A., Fini, L., Puglisi, A. T., Pinna, E., Xompero, M., Briguglio, R., Quirós-Pacheco, F., Stefanini, P., and Guerra, J. C. et al., "First Light AO (FLAO) System for LBT: Final Integration, Acceptance Test in Europe, and Preliminary On-Sky Commissioning Results," *Proceedings of SPIE*, Vol. 7736, Adaptive Optics Systems II, July 2010, Paper 773609.

[18] Close, L. M., , Males, J., Morzinski, K., Kopon, D., Follette, K., Rodigas, T., Hinz, P., Wu, Y., Puglisi, A., and Esposito, S.et al., "Diffraction-Limited Visible Light Images of Orion Trapezium Cluster with the Magellan Adaptive Secondary AO System (MagAO)," *Astrophysical Journal*, Vol. 774, No. 2, 2013, p. 94. doi:10.1088/0004-637X/774/2/94

[19] Foy, R., and Labeyrie, A., "Feasibility of Adaptive Telescope with Laser Probe," *Astronomy and Astrophysics*, Vol. 152, No. 1, 1985, pp. 129–131.

[20] Thompson, L. A., and Gardner, C. S., "Experiments on Laser Guide Stars at Mauna Kea Observatory for Adaptive Imaging in Astronomy," *Nature*, Vol. 328, No. 6127, 1987, pp. 229–231. doi:10.1038/328229a0

[21] Fugate, R. Q., Wopat, L. M., Fried, D. L., Ameer, G. A., Browne, S. L., Roberts, P. H., Tyler, G. A., Boeke, B. R., and Ruane, R. E., "Measurement of Atmospheric Wavefront Distortion Using Scattered Light from a Laser Guide-Star," *Nature*, Vol. 353, No. 6340, Sept. 1991, pp. 144–146. doi:10.1038/353144a0

[22] Lloyd-Hart, M., Angel, J. R. P., Jacobsen, B., Wittman, D., Dekany, R., McCarthy, D., Kibblewhite, E., Wild, W., Carter, B., and Beletic, J., "Adaptive Optics Experiments Using Sodium Laser Guide Stars," *Astrophysical Journal*, Vol. 439, No. 1, 1995, pp. 455–473. doi:10.1086/175187

[23] Max, C. E., , Olivier, S. S., Friedman, H. W., An, J., Avicola, K., Beeman, B. V., Bissinger, H. D., Brase, J. M., Erbert, G. V., and Gavel, D. T.et al., "Image Improvement from a Sodium-Layer Laser Guide Star Adaptive Optics System," *Science*, Vol. 277, No. 5332, 1997, pp. 1649–1652. doi:10.1126/science.277.5332.1649

[24] Wizinowich, P. L., , Le Mignant, D., Bouchez, A. H., Campbell, R. D., Chin, J. C., Contos, A. R., van Dam, M. A., Hartman, S. K., Johansson, E. M., and Lafon, R. E.et al., "The WM Keck Observatory Laser Guide Star Adaptive Optics System: Overview," *Publications of the Astronomical Society of the Pacific*, Vol. 118, No. 840, 2006, pp. 297–309. doi:10.1086/pasp.2006.118.issue-840

[25] Young, J., Haniff, C., and Buscher, D., "Interferometric Imaging of Geo-Synchronous Satellites with Ground-Based Telescopes," *IEEE Aerospace Conference*, IEEE Publ., Piscataway, NJ, March 2013, p. 9.

[26] Leclair, R. A., and Sridharan, R., "Probability of Collision in the Geostationary Orbit," *Proceedings of the 3rd European Conference on Space Debris*, edited by Sawaya-Lacoste, H., Vol. 1, ESA Special Publ. SP-473, Noordwijk, The Netherlands, March 2001, pp. 463–470.

[27] Skinner, M. A., et al., "Commercial Space Situational Awareness: An Investigation of Ground-Based SSA Concepts to Support Commercial GEO Satellite Operators," *Proceedings of the Advanced Maui Optical and Space Surveillance Technologies Conference*, Maui Economic Development Board, Maui, Sept. 2013, pp. 90–99.

[28] Jehn, R., Agapov, V., and Hernández, C., "End-of Disposal of Geostationary Satellites," *Proceedings of the 4th European Conference on Space Debris*, edited by Danesy, D., ESA SP-587, Darmstadt, Germany, Aug. 2005, p. 373.

[29] Space-Track, https://www.space-track.org [retrieved 17 Feb. 2016].

[30] Albert, J., "Satellite-Mounted Light Sources as Photometric Calibration Standards for Ground-Based Telescopes," *Astronomical Journal*, Vol. 143, No. 1, 2012, p. 8. doi:10.1088/0004-6256/143/1/8

[31] Hope, D., Jefferies, S., and Giebink, C., "Imaging Geo-Synchronous Satellites with the AEOS Telescope," *Proceedings of the Advanced Maui Optical and Space Surveillance Technologies Conference*, Maui Economic Development Board, Maui, 2008, pp. 304–311.

[32] Anon., "Request for Information: Technology Solutions for Passive, Sparse Aperture Imaging for Space Domain Awareness," Defense Advanced Research Projects Agency DARPA-SN-15-38, 2015.

[33] Guyon, O., "Limits of Adaptive Optics for High-Contrast Imaging," *Astrophysical Journal*, Vol. 629, No. 1, 2005, pp. 592–614. doi:10.1086/apj.2005.629.issue-1

[34] Ross, T. S., "Limitations and Applicability of the Maréchal Approximation," *Applied Optics*, Vol. 48, No. 10, 2009, pp. 1812–1818. doi:10.1364/AO.48.001812

[35] Rampy, R., Gavel, D., Rochester, S., and Holzlöhner, R., "Investigations of Long Pulse Sodium Laser Guide Stars," *Proceedings of SPIE*, Vol. 8447, Adaptive Optics Systems III, Sept. 2012, Paper 84474L.
[36] Denman, C. A., Drummond, J. D., Eickhoff, M. L., Fugate, R. Q., Hillman, P. D., Novotny, S. J., and Telle, J. M., "Characteristics of Sodium Guidestars Created by the 50-Watt FASOR and First Closed-Loop AO Results at the Starfire Optical Range," *Society of Photo-Optical Instrumentation Engineers (SPIE) Conference Series*, Vol. 6272, Proceedings of SPIE, July 2006, Paper 62721L. doi:10.1117/12.695916
[37] Beckers, J. M., "Increasing the Size of the Isoplanatic Patch with Multiconjugate Adaptive Optics," *Proceedings of a ESO Conference on Very Large Telescopes and Their Instrumentation*, edited by Ulrich, M.-H., Vol. 30, European Southern Observatory, Garching, March 1988, p. 693.
[38] Gavel, D. T., "Tomography for Multiconjugate Adaptive Optics Systems Using Laser Guide Stars," *Proceedings of SPIE*, Vol. 5490, SPIE Astronomical Telescopes and Instrumentation, Glasgow, Scotland, June 2004.
[39] Ammons, S. M., Johnson, L., Laag, E. A., Kupke, R., Gavel, D. T., Bauman, B. J., and Max, C. E., "Integrated Laboratory Demonstrations of Multi-Object Adaptive Optics on a Simulated 10 Meter Telescope at Visible Wavelengths," *Publications of the Astronomical Society of the Pacific*, Vol. 122, No. 891, May 2010, pp. 573–589. doi:10.1086/649001
[40] Greenaway, A. H., "Space Astronomical Telescopes and Instruments," *Proceedings of SPIE*, Vol. 1494, SPIE, Sept. 1991, p. 8.
[41] Greenaway, A. H., and Clark, S. E., "PHAROS: An Agile Satellite-Borne Laser Guidestar," *Proceedings of SPIE 2120, Laser Beam Propagation and Control*, Vol. 206, June 1994, pp. 206–210. doi:10.1117/12.177692
[42] Hand, E., "Startup Liftoff," *Science*, Vol. 348, No. 6231, April 2015, pp. 172–177. doi:10.1126/science.348.6231.172
[43] Planetary Systems Corporation, http://www.planetarysystemscorp.com/?post_type=product&p=448 [retrieved 21 April 2015].
[44] Anon., "American National Standard for Safe Use of Lasers," American National Safety Inst., ANSI Z136.1, 2014.
[45] Morzinski, K. M., Close, L. M., Males, J. R., Hinz, P. M., Esposito, S., Riccardi, A., Briguglio, R., Follette, K. B., Pinna, E., and Puglisi, A. et al., "MagAO: Status and Science," *Proceedings of SPIE*, Vol. 9909, Adaptive Optics Systems V, Sept. 2016, Paper 990901.
[46] Males, J. R., , Close, L. M., Morzinski, K. M., Wahhaj, Z., Liu, M. C., Skemer, A. J., Kopon, D., Follette, K. B., Puglisi, A., and Esposito, S. et al., "Magellan Adaptive Optics First-Light Observations of the Exoplanet β Pic b. I. Direct Imaging in the Far-Red Optical with MagAO + VisaAO and in the Near-IR with NICI," *Astrophysical Journal*, Vol. 786, No. 1, 2014, p. 32. doi:10.1088/0004-637X/786/1/32
[47] Males, J. R., , Close, L. M., Guyon, O., Morzinski, K. M., Hinz, P., Esposito, S., Pinna, E., Xompero, M., Briguglio, R., and Riccardi, A. et al., "The Path to Visible Extreme Adaptive Optics with MagAO-2K and MagAO-X," *The Future of Photometric, Spectrophotometric and Polarimetric Standardization, ASP Conference Series*, edited by Sterken, C., Vol. 364, Astronomical Soc. of the Pacific, San Francisco, 2007, p. 315.
[48] Males, J.et al., "The Path to Visible Extreme Adaptive Optics with MagAO-2K and MagAO-X," *Proceedings of SPIE*, Vol. 9909, Adaptive Optics Systems V, July 2016, Paper 990952.
[49] Tokovinin, A., "Adaptive Optics Tutorial at CTIO," May 2001, http://www.ctio.noao.edu/~atokovin/tutorial/intro.html [accessed Sept. 2015].
[50] Le Mignant, D., , van Dam, M. A., Bouchez, A. H., Chin, J. C., Chock, E., Campbell, R. D., Conrad, A., Doyle, S., Goodrich, R. W., and Johansson, E. M.et al., "LGS AO at WM Keck Observatory: Routine Operations and Remaining Challenges," *SPIE Astronomical* Telescopes + Instrumentation, International Soc. for Optics and Photonics Paper 627201, June 2006.
[51] Wertz, J. R., and Larson, W. J., *Space Mission Analysis and Design*, 3rd ed., Microcosm Press, Hawthorne, CA, Oct. 1999.
[52] Analytical Graphics, Inc. STK Website, http://www.agi.com/products/stk/.
[53] Hemmati, H., *Near-Earth Laser Communications*, Hemmati Publ., Baton Rouge, FL, 2009, Chaps. 3, 4, 8.
[54] Carroll, K. A., Rucinski, S., and Zee, R. E., "Arc-Minute Nanosatellite Attitude Control: Enabling Technology for the BRITE Stellar Photometry Mission," *Small Satellite Conference*, 2004, Paper SSC04-V-2.
[55] Janson, S. C., and Welle, R. P., "The NASA Optical Communication and Sensor Demonstration Program: An Update," *Small Satellite Conference*, SSC14-VI-1, 2014, p. 10.
[56] Roberts, L. C., Burruss, R., Fregoso, S., Herzog, H., Piazzola, S., Roberts, J. E., Spiers, G. D., and Truong, T. N., "The Adaptive Optics and Transmit System for NASA's Laser Communications Relay Demonstration Project," *SPIE Optical Engineering+ Applications*, International Soc. for Optics and Photonics Paper 99790I, Sept. 2016.
[57] ThorLabs, "TPA850P10—850 nm Tapered Amplifier, 1 W, 20 nm BW, Butterfly Pkg, PM Fiber, FC/APC," 2016, https://www.thorlabs.com/thorproduct.cfm?partnumber=TPA850P10 [accessed May 2016].
[58] Saleh, B. E. A., and Teich, M. C., "Nonlinear Optics," *Fundamentals of Photonics*, 2nd ed., Wiley, Hoboken, NJ, 2007, pp. 875–917.
[59] Thorlabs, "Periodically Poled Lithium Niobate (PPLN)—Tutorial," Thorlabs Tech. Rept., pp. 686–693, https://www.thorlabs.com/catalogpages/693.pdf [accessed Aug. 2016].
[60] Paschotta, R., "Frequency Doubling," *RP Photonics Encyclopedia*, March 2016, https://www.rp-photonics.com/frequency_doubling.html [accessed April 2016].
[61] Coherent Inc., "Mira-OPOX, an Optical Parametric Oscillator (OPO)," https://www.coherent.com/lasers/laser/mira-opo [accessed May 2016].
[62] "Canisterized Satellite Dispenser," CSD Data Sheet PSC Document 2002337, Planetary Systems Corp., 2014, http://www.planetarysystemscorp.com/ [accessed Nov. 2015].
[63] Mehrparvar, A., "CubeSat Design Specification, Rev 13," April 2015, http://cubesat.calpoly.edu/images/developers/cds_rev13_final.pdf [accessed Sept. 2015].
[64] Shimmin, R., "Small Spacecraft Technology State of the Art," NASA Ames Research Center, Mission Design Division, NASA/TP-2015-216648/REV1, 2015.
[65] Grimes, J., "Global Positioning System Standard Positioning Service Performance Standard," Department of Defense, Global Positioning System, Tech. Rept., Sept. 2008, http://www.gps.gov/technical/ps/2008-SPS-performance-standard.pdf [accessed March 2016].
[66] Kelso, T., "NORAD Two-Line Element Set Format," May 2014, http://celestrak.com/NORAD/documentation/tle-fmt.asp [accessed May 2015].
[67] https://www.space-track.org/ [accessed Oct. 2015].
[68] Hoots, F. R., and Roehrich, R. L., "Models for Propagation of NORAD Element Sets," U.S. Department of Defense Spacetrack Report, Tech. Rept., Dec 1998, http://www.celestrak.com/NORAD/documentation/spacetrk.pdf [accessed March 2016].
[69] Blue Canyon Technologies, "BCT XACT Data Sheet," 2016, http://bluecanyontech.com/wp-content/uploads/2016/08/ADCS_F.pdf [accessed Aug. 2016].
[70] Maryland Aerospace Inc., "MAI-400 Reaction Wheel," 2016, http://maiaero.com/datasheets/MAI400_Specifications.pdf [accessed Aug. 2016].
[71] Sinclair Interplanetary, "Reaction Wheels," 2016, http://www.sinclairinterplanetary.com/reactionwheels [accessed Dec. 2015].
[72] Busek Co. Inc., "Busek Electrospray Thrusters," 2015, http://www.busek.com/technologies__espray.htm [accessed May 2015].
[73] Accion Systems Inc., "MIN-0 25cc CubeSat Propulsion and Attitude Control," 2016, http://www.accion-systems.com/technology/#accion-tech [accessed Dec. 2015].
[74] Vacco Industries, "Standard Micro CubeSat Propulsion System," Sept. 2015, http://www.vacco.com/images/uploads/pdfs/MicroPropulsionSystems_0714.pdf [accessed Sept. 2015].
[75] Busek Co. Inc., "BIT-3 RF Ion Thruster," 2013, http://www.busek.com/technologies__ion.htm [accessed Sept. 2015].
[76] Tsay, M., "Intro to High-Performance Propulsion Systems for Nano/MicroSats," Massachusetts Inst. of Technology, Sept. 2015.
[77] Busek Co. Inc., "Green Monopropellant Thrusters," *Space Propulsion and Systems*, 2014, http://www.busek.com/index_htm_files/70008517C.pdf [accessed May 2016].
[78] Pumpkin Inc., "CubeSat Kit," 2013, http://www.cubesatkit.com/content/kits.html [accessed May 2016].
[79] Innovation Solutions In Space, "Satellite Products: Structures," 2016, http://www.isispace.nl/product-category/satellite-products/structures/ [accessed May 2016].
[80] McComas, D., "NASA/GSFC's Flight Software Core Flight System," *Flight Software Workshop*, Invited talk at the Flight Software Workshop, Southwest Research Inst., San Antonio, TX, Nov. 2012, http://flightsoftware.jhuapl.edu/files/2012/FSW12_Fesq_Dvorak.pdf.
[81] American Institute of Aeronautics, and Astronautics, "Standard: Space Plug-and-Play Architecture," AIAA Standards AIAA S-133-2-2013, 2013. doi:10.2514/4.102301.001
[82] Klofas, B., "CubeSat Communications System Table," http://klofas.com/comm-table/ [accessed May 2016].
[83] Ammanii, M., and Chen, Z. N., "Wideband Monopole Antennas for Multi-Band Wireless Systems," *IEEE Antennas and Propagation Magazine*, Vol. 45, No. 2, 2003, pp. 146–150.

[84] Holdaway, B., "The Space Plug-and-Play Architecture Services Manager and Its Relevance in Diverse Plug-and-Play Software Systems," 2014, Paper 407.

[85] Syrlinks, "X-Band Transmitter can Transmit up to 13.3 GB per Pass with a 5 m Station, Designed for CubeSat and NanoSatellites (LEO)," 2016, http://www.syrlinks.com/en/products/cubesats/hdr-x-band-transmitter.html [accessed May 2015].

[86] Schaire, S., "Wallops CubeSat-SmallSat Ground Stations and Frequency Standardization," *Presented at the Cubesat Developers Workshop*, April 2013, http://mstl.atl.calpoly.edu/~bklofas/Presentations/DevelopersWorkshop2013/GroundStation_Workshop_Schaire_Wallops_ Standardization.pdf.

[87] Poker Flat Research Range, "Welcome to Poker Flat," http://www.pfrr.alaska.edu/ [accessed Dec. 2015].

[88] Anon., "State of the Satellite Industry Report," The Tauri Group, Tech. Rept., 2015, http://www.sia.org/wp-content/uploads/2015/06/Mktg15-SSIR-2015-FINAL-Compressed.pdf [accessed Oct. 2015].

[89] Spaceflight, "Schedule & Pricing," 2016, http://www.spaceflight.com/schedule-pricing/ [accessed May 2016].

J. A. Christian
Associate Editor